

A numerical investigation of continental collision styles

Reza Khabbaz Ghazian^{1,2} and Susanne J. H. Buiter^{1,2}

¹Geodynamics Team, Geological Survey of Norway (NGU), Leiv Eirikssons vei 39, 7040 Trondheim, Norway. E-mail: rezg@statoil.com

²University of Oslo, PO. 1072 Blindern, 0316 Oslo, Norway

Accepted 2013 February 14. Received 2013 February 10; in original form 2012 August 31

SUMMARY

Continental collision after closure of an ocean can lead to different deformation styles: subduction of continental crust and lithosphere, lithospheric thickening, folding of the unsubducted continents, Rayleigh–Taylor (RT) instabilities and/or slab break-off. We use 2-D thermomechanical models of oceanic subduction followed by continental collision to investigate the sensitivity of these collision styles to driving velocity, crustal and lithospheric temperature, continental rheology and the initial density difference between the oceanic lithosphere and the asthenosphere. We find that these parameters influence the collision system, but that driving velocity, rheology and lithospheric (rather than Moho and mantle) temperature can be classified as important controls, whereas reasonable variations in the initial density contrast between oceanic lithosphere and asthenosphere are not necessarily important. Stable continental subduction occurs over a relatively large range of values of driving velocity and lithospheric temperature. Fast and cold systems are more likely to show folding, whereas slow and warm systems can experience RT-type dripping. Our results show that a continent with a strong upper crust can experience subduction of the entire crust and is more likely to fold. Accretion of the upper crust at the trench is feasible when the upper crust has a moderate to weak strength, whereas the entire crust can be scraped-off in the case of a weak lower crust. We also illustrate that weakening of the lithospheric mantle promotes RT-type of dripping in a collision system. We use a dynamic collision model, in which collision is driven by slab pull only, to illustrate that adjacent plates can play an important role in continental collision systems. In dynamic collision models, exhumation of subducted continental material and sediments is triggered by slab retreat and opening of a subduction channel, which allows upward flow of buoyant materials. Exhumation continues after slab break-off by reverse motion of the subducting plate ('eduction') caused by the reduced slab pull. We illustrate how a simple force balance of slab pull, slab push, slab bending, viscous resistance and buoyancy can explain the different collision styles caused by variations in velocity, temperature, rheology, density differences and the interaction with adjacent plates.

Key words: Numerical solutions; Subduction zone processes; Continental margins: convergent; Dynamics of lithosphere and mantle; Mechanics, theory, and modeling.

1 INTRODUCTION

Continent–continent collision occurs when an intervening ocean has been closed by subduction of the oceanic lithosphere. Continental collision systems in the Himalayas, European Alps, Norwegian Caledonides and Zagros show that this process can be accompanied by crustal thickening, magmatism, metamorphism, the formation of thrust nappes and high topography, and the exhumation of (ultra-) high pressure [(U)HP] rocks from large depths (Dewey & Burke 1973; Molnar & Tapponnier 1975; Pfiffner *et al.* 1990; Andersen *et al.* 1991; Blanc *et al.* 2003; Leech *et al.* 2005). UHP rocks record pressures of up to 2–3.5 GPa and temperatures of up to 600–800 °C (Andersen *et al.* 1991; Jamtveit *et al.* 1991; Hacker

2006; Hacker *et al.* 2010). They are exhumed during subduction or collision through mechanisms that are still debated, but that may likely combine internal drivers, such as, buoyancy differences, and external drivers, such as, reverse motion in the subduction channel, crustal-scale extension and squeezing of weak material between two stronger blocks (Warren 2013). Previous studies have pointed out that continental collision can be accommodated in different styles (Houseman & Molnar 1997; Cloetingh *et al.* 1999; Burg & Podladchikov 2000; Toussaint *et al.* 2004a, Fig. 1): (1) Stable subduction of continental lithosphere: Even though continental lithosphere is positively buoyant, continental material has been interpreted to have subducted to depths of 100–250 km (Andersen *et al.* 1991; Ye *et al.* 2000; Ding *et al.* 2003). Continental lithosphere could, for

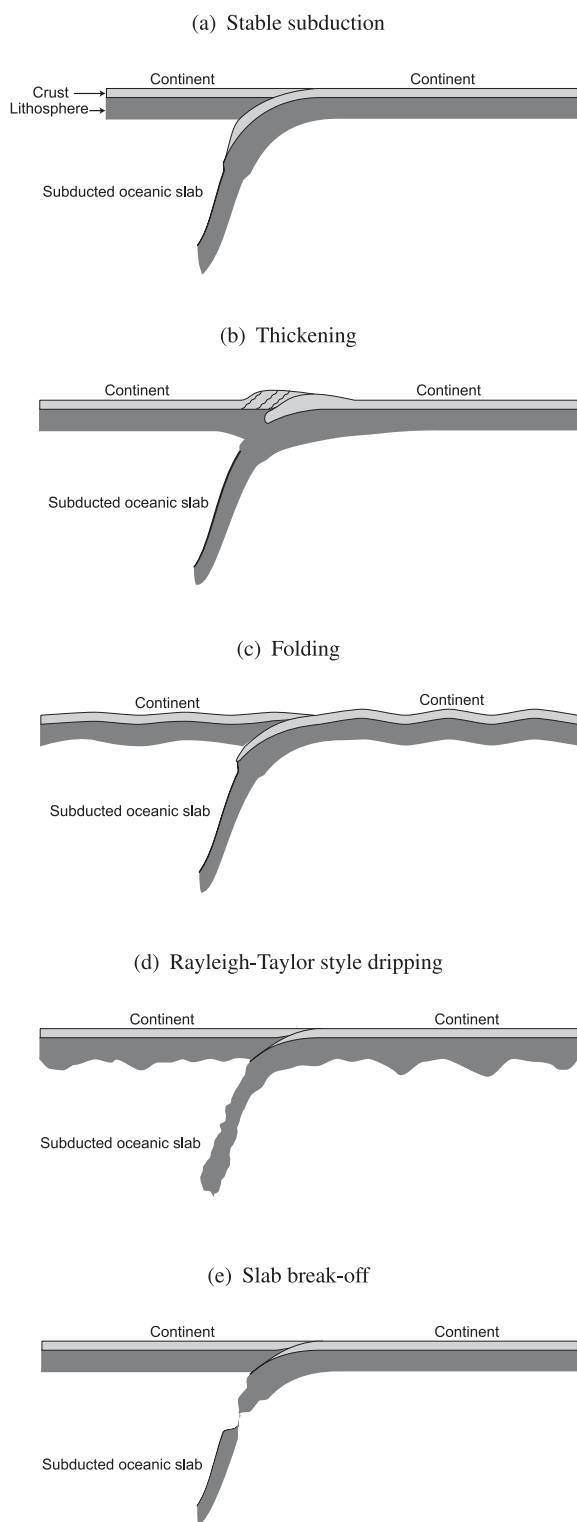


Figure 1. Cartoons illustrating different styles of deformation in a continental collision system.

example, be pulled down entirely by an attached negatively buoyant oceanic slab. Or the overall positive buoyancy of the continental lithosphere could be reduced by offscraping part of the continental crust at the trench or delaminating the mantle lithosphere from the crust (Bird 1979), which would facilitate subduction of the remaining thinned crust and underlying lithospheric mantle. Continental subduction is favoured for systems in which the continent is strong,

driving velocity is high and the subduction fault (or channel) is weak (Toussaint *et al.* 2004a; Selzer *et al.* 2008). (2) Thickening of crust and lithosphere: Most collision systems experience crustal thickening as evidenced by a deep Moho. This thickening is accommodated by faulting, formation of nappes and/or a pure-shear style of deformation (Tapponnier *et al.* 1986; Roecker *et al.* 1987; Andersen *et al.* 1991). (3) Lithospheric-scale folding: This is a basic response of the continental plate to large-scale shortening which becomes feasible when there is a strong coupling between crust and mantle and/or a strong subduction fault (Burg & Podladchikov 2000; Toussaint *et al.* 2004a; Luth *et al.* 2010). (4) Rayleigh–Taylor (RT) instabilities: Continents with a weak lithospheric mantle, either because of a warm geotherm or because of weak rheological properties, can experience RT-type of lithospheric dripping (Houseman & Molnar 1997; Pysklywec *et al.* 2000; Toussaint *et al.* 2004a). (5) Slab break-off: If the transition from subduction to continent–continent collision is accompanied by subduction of positively buoyant continental crust and/or locking of the interplate contact, a resistance to slab pull arises that can lead to an extensional regime in the subducted slab, which can cause slab break-off (Davies & von Blanckenburg 1995; Li & Liao 2002). Slab break-off has been inferred from gaps in the hypocentral distribution of seismicity within subducted slabs (Barazangi *et al.* 1973; Pascal *et al.* 1973; Fuchs *et al.* 1979) and from low-velocity regions in tomographic images (Wortel & Spakman 2000; Hafkenscheid *et al.* 2006). The process is associated with syn-collision magmatism, surface uplift and exhumation of UHP rocks (Davies & von Blanckenburg 1995; Buiter *et al.* 2002; Gerya *et al.* 2004; Andrews & Billen 2007; Duretz *et al.* 2011).

Using upper-mantle-scale viscous–plastic numerical experiments, Pysklywec *et al.* (2000) showed that plate driving velocity is a primary controlling factor for the deformation style of a collision system. They found that RT-type of dripping is a dominant mechanism for slow systems, whereas stable subduction becomes more dominant with increasing driving velocity. Toussaint *et al.* (2004a,b) (see also Burov & Yamato 2008) also employed numerical models on the scale of the upper mantle and showed that the style of collision strongly depends on both driving velocity and continental temperature (parametrized as temperature of the Moho). They found that continental subduction is favoured for strong lithospheres ($T_{\text{Moho}} < 550^\circ\text{C}$) and fast initial driving velocity ($>3\text{--}5\text{ cm yr}^{-1}$). Pure-shear thickening and lithospheric folding become dominant when the lithosphere is weak because of a warmer geotherm ($550^\circ\text{C} < T_{\text{Moho}} < 650^\circ\text{C}$) or a slower driving velocity ($<5\text{ cm yr}^{-1}$), which allows the lithosphere to warm up by heat conduction. RT-type of instabilities occur only in hot systems ($T_{\text{Moho}} > 800^\circ\text{C}$), in which high temperatures reduce the effective viscosity of the continental lithosphere, but the lithosphere still remains denser than the asthenosphere, resulting in a high instability growth rate. In addition, the rheology of the lower crust may also have a significant effect on continental subduction and the tendency for folding (Toussaint *et al.* 2004a). A strong lower crust increases the coupling between upper crust and lithospheric mantle and results in a system that is more likely to experience folding. A strong lower crust also promotes subduction of the upper crust in a situation of stable subduction, whereas the upper crust can detach and accumulate at the surface or at mid-crustal depths for continents with a weak lower crust (Pysklywec & Cruden 2004; De Franco *et al.* 2008; Faccenda *et al.* 2008; Luth *et al.* 2010). Other factors that could be thought to play a role in controlling the style of continental collision are the rheology of the upper crust and the lithospheric mantle, slab dip (flat slab versus steep slab subduction), the strength of the interface between the converging plates, the role of adjacent plates versus slab pull,

surface processes (erosion and sedimentation), buoyancy, melting and phase changes (von Blanckenburg & Davies 1995; Ranalli *et al.* 2000; Pysklywec 2006; Billen & Hirth 2007; De Franco *et al.* 2008; Selzer *et al.* 2008; Warren *et al.* 2008; Luth *et al.* 2010; Li *et al.* 2011).

Previous numerical models of continental collision have often focused on crustal and lithospheric-scale structures in models with a simplified mantle representation (Beaumont *et al.* 1996; Stockmal *et al.* 2007; Selzer *et al.* 2008) or on the dynamics of the whole system on the scale of at least the upper mantle (Pysklywec *et al.* 2000; Toussaint *et al.* 2004a; Burov & Yamato 2008). Lithosphere-scale models allow a high resolution that can resolve thrust and nappes, but need to simulate mantle behaviour with boundary conditions. Many subduction models on the scale of the upper mantle have in turn more limited resolution in the crust and lithosphere and sometimes employ a free-slip surface boundary, which suppresses the development of vertical topography (e.g. Capitanio *et al.* 2009; van Hunen & Allen 2011).

In this study, we investigate crustal- and lithospheric-scale deformation in combination with mantle dynamics through numerical models that have a free upper surface and a reasonable resolution (2×2 km per element) in the lithosphere. We aim to investigate the sensitivity of collision styles to driving velocity, lithospheric temperature, the strength stratification of the continents, forcing by adjacent plates, and the initial density difference between the oceanic lithospheric mantle and the sub-lithospheric mantle. Our 2-D models are driven by a combination of slab pull and a kinematic lateral boundary condition that simulates the effects of ridge push and movements of surrounding plates. The kinematic condition is maintained during collision, resulting in a kinematically driven collision style. We study the role of adjacent plates on collision styles with a model in which the kinematic boundary condition is removed once the system is self-sustaining (Baumann *et al.* 2010). This simulates a collision system isolated from surrounding plates, which we call a dynamic collision model.

2 NUMERICAL APPROACH

2.1 Modelling method

We solve the standard equations for conservation of mass, momentum and energy for incompressible slow creeping flows:

$$\nabla \cdot \mathbf{u} = 0, \quad (1)$$

$$\nabla \cdot \sigma' - \nabla P + \rho \mathbf{g} = 0, \quad (2)$$

$$\rho c_p \left(\frac{\partial T}{\partial t} + \mathbf{u} \cdot \nabla T \right) = k \nabla^2 T + Q, \quad (3)$$

where \mathbf{u} is the velocity vector, σ' the deviatoric stress tensor, P dynamic pressure (mean stress), ρ density, \mathbf{g} gravitational acceleration ($g_x = 0$, $g_y = -9.8$ m s⁻²), c_p specific heat, T temperature, t time, k thermal conductivity and Q heat generation. We ignore shear heating. We use the 2-D version of the numerical code SULEC v3.4, which uses the Arbitrary Lagrangian–Eulerian (ALE) finite element method. Pressure is solved using the iterative penalty method (Cuvelier 1986; Pelletier *et al.* 1989; Zienkiewicz & Taylor 2000), in which the continuity eq. (1) is perturbed as following:

$$P^{\text{new}} = P^{\text{old}} - \kappa \nabla \cdot \mathbf{u}, \quad (4)$$

where κ is the compressibility factor (generally taken eight orders of magnitude larger than the largest viscosity in the model,

Zienkiewicz & Taylor 2000). The perturbed continuity eq. (4) and the momentum eq. (2) are solved in an iterative way to minimize the norms of two successive velocity and pressure values to the desired tolerance. Eqs (2)–(4) are solved on an Eulerian grid which can be vertically stretched or shrunk to accommodate free surface displacements (Fallsack 1995). Our models have a true free surface which includes a stabilization term to suppress numerical overshoot across interfaces with large density contrasts (Kaus *et al.* 2010; Quinquis *et al.* 2011). At the surface, diffusive erosion and sedimentation is applied with a diffusion coefficient of 5×10^{-6} m² s⁻¹ (Culling 1960). We use a quadrilateral element with four velocity nodes (with two degrees of freedom each) and constant pressure, which gives continuous velocity and discontinuous pressure between elements. Material properties are stored on markers which are advected at the end of each time step. We use the extended Boussinesq approach, in which density is temperature-dependent.

$$\rho = \rho_0(1 - \alpha(T - T_0)), \quad (5)$$

where ρ_0 is the density at temperature T_0 and α is the coefficient of volume expansion. SULEC uses the direct solver PARDISO (Schenk & Gärtner 2004) to solve the mechanical and thermal equations.

In our models, materials deform by viscous flow or brittle behaviour, as determined by the mechanism that requires least effective stress. Viscous behaviour is described by a power-law relation of viscosity, strain-rate, pressure and temperature

$$\eta = s_c \frac{1}{2} A^{-\frac{1}{n}} \dot{\epsilon}_{II}^{\left(\frac{1}{n}-1\right)} d^{\frac{p}{n}} C_{OH}^{-\frac{r}{n}} e^{\left(\frac{E+PV}{nRT}\right)}, \quad (6)$$

where η is viscosity, s_c a scaling factor, A a constant, $\dot{\epsilon}_{II}$ effective strain-rate [$\dot{\epsilon}_{II} = \left(\frac{1}{2}\dot{\epsilon}_{ij}\dot{\epsilon}_{ij}\right)^{\frac{1}{2}}$], n stress exponent, d grain size, p grain size exponent, C_{OH} water content, r water exponent, E activation energy, V activation volume and R the gas constant. We use dislocation creep flow laws of wet quartzite (Gleason & Tullis 1995) for the upper continental crust, wet anorthite (Rybacki *et al.* 2006) for the lower continental crust, gabbro (Wilks & Carter 1990) for the oceanic crust and wet olivine (Hirth & Kohlstedt 2003) for the oceanic and continental lithospheric mantle. For the sublithospheric mantle, we use composite dislocation and diffusion creep of wet olivine (Hirth & Kohlstedt 2003). In the latter case, it is assumed that both the dislocation (dis) and diffusion (diff) mechanisms of olivine provide a portion of the total deformation. The composite (comp) viscosity is computed from (van den Berg *et al.* 1993)

$$\frac{1}{\eta_{\text{comp}}} = \frac{1}{\eta_{\text{dis}}} + \frac{1}{\eta_{\text{diff}}}. \quad (7)$$

Brittle behaviour is described by the Drucker–Prager relation

$$\sigma'_{II} = P \sin \phi + C \cos \phi, \quad (8)$$

where σ'_{II} is the effective deviatoric stress [$\sigma'_{II} = \left(\frac{1}{2}(\sigma'_{ij}\sigma'_{ij})\right)^{\frac{1}{2}}$], ϕ angle of internal friction, C cohesion and P dynamic pressure. We use linear softening of the angle of internal friction from ϕ_1 to ϕ_2 in an interval of finite strain values (0.5–1.0), described by the second invariant of the strain tensor [$\epsilon_{II} = \left(\frac{1}{2}(\epsilon_{ij}\epsilon_{ij})\right)^{\frac{1}{2}}$], as a mechanism for localization of strain in our models (Beaumont *et al.* 1996). This simulates the effects of mineral transformations, development of foliation or grain size changes that can occur in natural shear zones (Mandl 1988; Rice 1992; Bos & Spiers 2002). The magnitude of the softening of the angle of internal friction follows Bos & Spiers (2002) who suggest a decrease in friction coefficient by approximately a factor 2, based on a microphysical model for shear deformation of foliated, phyllosilicate-bearing fault rock. An

alternative approach to achieve localization of deformation in numerical models is through the introduction of shear heating (Regenauer-Lieb & Yuen 2003). This softening mechanism operates on the viscous deformation field, whereas our strain softening operates on the brittle field. The effectiveness of shear heating can be seen from the dimensionless number L_0 (Kaus & Podladchikov 2006; Braeck *et al.* 2009; Cramer & Kaus 2010), whereby localization through shear heating is effective if $L_0 \geq 1$.

$$L_0 = \frac{\dot{\epsilon}_{bg} L}{1.4} \sqrt{\frac{\eta_0 E}{n R T_0^2 k}}, \quad (9)$$

where $\dot{\epsilon}_{bg}$ is the background strain-rate, L characteristic length of heterogeneity, and η_0 the viscosity at reference temperature T_0 . E , n , R and k are as above in eqs (3) and (6). All parameters of this equation are known for a specific model set-up, except L . Cramer & Kaus (2010) pointed out that localization could be predicted if L is considered as the brittle thickness of the lithosphere. Substitution of corresponding values from Table 1, using a characteristic length L of 20 km, and a background strain-rate of 10^{-15} s^{-1} results in a value less than one. Shear heating may, therefore, play a role in models similar to ours, but is not expected to represent a dominant process for our set-up. All rheological and thermal parameters are listed in Table 1.

2.2 Model set-up

Our model is 2000 km wide by 660 km deep and contains two continents with an intervening ocean (Fig. 2a). Tests with model domains up to 3000 km width (for the same depth of 660 km) show the same subduction and collision evolution, confirming that the width of 2000 km is sufficient for our models. The oceanic slab is about to start subduction and to initiate this, the model has a weak seed wide enough (~ 4 –5 elements) to localize strain along the leftmost continent–ocean interface. The dip of the seed and its adjacent continent–ocean interface is 38° . This dip angle leads to a steeply dipping subducted slab in our models, similar to other

models showing that initial conditions can impact slab dip angle during later evolution stages (Buiter & Ellis 2010; Li *et al.* 2011). The continents have a 20-km thick upper crust, 20-km thick lower crust and 80-km thick lithospheric mantle overlying the sublithospheric mantle. The intervening ocean is initially 550 km wide and consists of an 8-km thick oceanic crust and a 72-km thick oceanic mantle lithosphere. We use a non-uniform mesh with a resolution which increases vertically upwards to reach 2 km in the crust and lithosphere. The highest horizontal resolution (2 km) is imposed around the trench where subduction and later collision is expected to happen. The total number of elements in our model is 338×124 and we use at least nine tracers in each element (377 208 tracers initially, a number which changes slightly because tracer injection or deletion keeps tracer density per element between 9 and 20).

The initial temperature of the continental domains is computed by solving the steady-state conductive heat equation (Chapman 1986). This results in a Moho temperature of 586°C and a lithospheric temperature at 120 km depth of 1300°C for our reference model. The oceanic domain has an initial geotherm determined from the plate cooling model (Turcotte & Schubert 2002) for a 60-Ma-old ocean (Fig. 2b). A transition zone provides a gradual change from the initial continental to oceanic geotherms. The temperature is held fixed at 0°C at the surface during model evolution. The heat flux is 25 mW m^{-2} at the bottom (at 660 km depth) and zero at the sides. The mantle adiabat is $0.3^\circ\text{C km}^{-1}$. We use a high thermal conductivity value ($k = 83.33 \text{ W m}^{-1} \text{ K}^{-1}$) for the sublithospheric mantle deeper than 120 km to keep the adiabatic mantle geotherm and heat flux into the base of the lithosphere nearly constant (Pysklywec & Beaumont 2004). Mantle above 120 km depth has a lower conductivity ($k = 2.3 \text{ W m}^{-1} \text{ K}^{-1}$).

We use two set-ups which differ in the displacement freedom of the continent on the subducting plate. In the reference model, the rightmost continent is pushed with an inward velocity (4 cm yr^{-1}) and the leftmost continent is held fixed. We call this the kinematically driven collision model (Fig. 2a). The velocity is applied along the side boundary to 120 km depth. This inflow is balanced by

Table 1. Rheological and thermal parameters of the models.

Layers	Continental upper crust	Continental lower crust	Continental lithosphere	Sediment	Oceanic crust	Oceanic lithosphere	Mantle	Upper seed	Lower seed	
Flow law	Wet quartzite ^a	Wet anorthite ^b	Wet olivine ^c dislocation	Wet quartzite ^a	Gabbro ^d	Wet olivine ^c dislocation	Wet olivine ^c composite diffusion dislocation	Gabbro ^d	Wet olivine ^c dislocation	
A^e ($\text{Pa}^{-n} \text{ s}^{-1} \text{ m}^p (\text{H}/10^6 \text{Si})^{-r}$)	1.40e-31	7.13e-18	5.33e-19	1.40e-31	1.12e-10	5.33e-19	1.50e-18	5.33e-19	1.12e-10	5.33e-19
n	4	3	3.5	4	3.4	3.5	1	3.5	3.4	3.5
E (J mol^{-1})	137e3	345e3	520e3	137e3	497e3	480e3	335e3	480e3	497e3	480e3
V ($\text{m}^3 \text{ mol}^{-1}$)	0	38e-6	11e-6	0	0	11e-6	4e-6	11e-6	0	11e-6
d (m)	0	0	0	0	0	0	5e-3	0	0	0
p	0	0	0	0	0	0	3	0	0	0
C_{OH} ($\text{H}/10^6 \text{Si}$)	0	200	50	0	0	200	200	200	0	200
r	0	1	1.2	0	0	1.2	1	1.2	0	1.2
ϕ_1	15°	15°	20°	10°	5°	20°	20°	5°	5°	5°
ϕ_2	7.5°	7.5°	10°	5°	2°	10°	10°	2°	2°	2°
C (Pa)	20e6	20e6	20e6	5e6	5e6	20e6	0	2e6	2e6	2e6
ρ_0 (kg m^{-3})	2800	2900	3240	2700	3100	3280	3250	3100	3240	3240
T_0 ($^\circ\text{C}$)	0	339	1300	0	0	1300	1300	0	1300	1300
α (K^{-1})	2e-5	2e-5	2e-5	2e-5	2e-5	2e-5	2e-5	2e-5	2e-5	2e-5
k ($\text{W m}^{-1} \text{ K}^{-1}$)	2.5	2.5	2.8	2.5	2.5	2.3	83.33	2.3	2.3	2.3
C_p ($\text{m}^2 \text{ K s}^{-2}$)	750	750	750	750	750	750	750	750	750	750
Q (W m^{-3})	0.58e-6	0.58e-6	0	0.58e-6	0	0	0	0	0	0

^a Gleason & Tullis (1995), ^b Rybacki *et al.* (2006), ^c Wilks & Carter (1990), ^d Hirth & Kohlstedt (2003).

^e Adjusted to a general state of stress (Ranalli 1995).

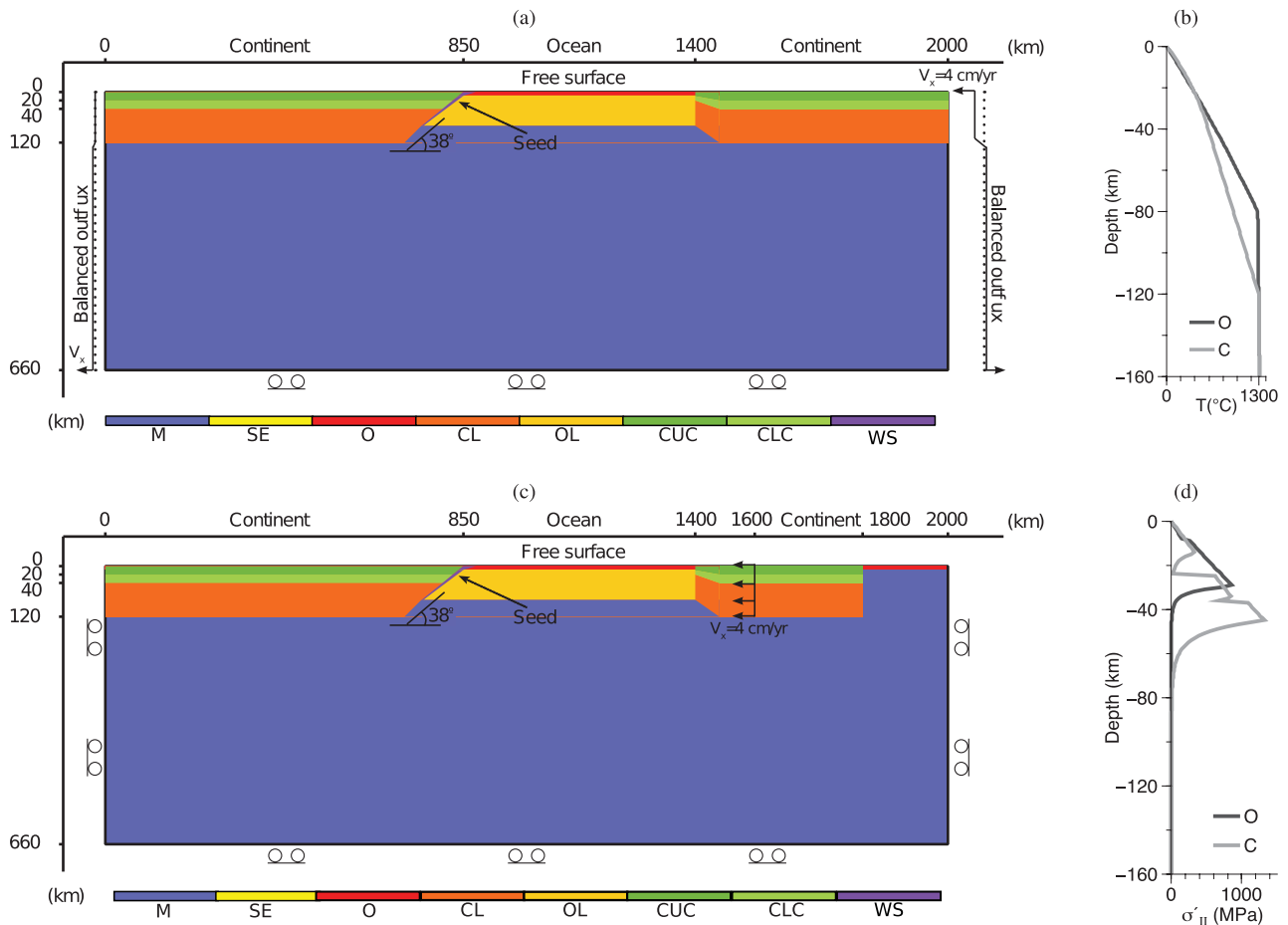


Figure 2. (a) Kinematically driven collision reference model set-up showing two continents with an intervening 60 Ma ocean. M, mantle; SE, sediment; O, oceanic crust; CL, continental lithosphere; OL, oceanic lithosphere; CUC, continental upper crust; CLC, continental lower crust; WS, weak seed. (b) Initial thermal profiles. O, ocean; C, continent. (c) Dynamic collision model set-up. (d) Initial effective stress profiles.

outflow on both side boundaries below the lithosphere (120–660 km). The change from inflow to outflow is applied gradually over four elements to avoid building up of high strains. The vertical component of velocity on the side boundaries is free. The model has a free slip boundary condition at the base and a true free surface at the top.

Our second set-up differs from the kinematically driven collision model in that the continent on the subducting plate now has a free right-hand side boundary (Fig. 2c). We call this model the dynamic collision model. The right-hand continent extends from $x = 1400$ – 1800 km and is therefore 200 km shorter than in the kinematically driven collision model. During the first steps of oceanic subduction, the continent grows by conversion of ocean to continental material at $x = 1800$ km. We simulate a very simple mid-ocean ridge at the top right-hand side of the model by enforcing oceanic crust formation in the domain from $x = 1800$ to 2000 km, with a 8-km thick oceanic crust which is underlain by mantle with a thermal conductivity of $2.3 \text{ W m}^{-1} \text{ K}^{-1}$ to 120 km depth. This material has an initial temperature equal to the mantle at 120 km depth (1300°C). The right-side boundary also has $T = 1300^\circ\text{C}$ from the surface to 120 km depth. In the initial stages of the model, an internal constant velocity (4 cm yr^{-1}) is applied within the right continent at $x = 1600$ km to start subduction. This velocity is removed when the system gained enough slab pull to be driven self-consistently. This is typically after 7 Myr of convergence.

Our two set-ups are end-members in the manner in which they address the interaction between the internal forces of slab pull and mantle flow and the external constraints supplied by surrounding plates. We realize that natural subduction zones will lie somewhere in between, but these end-members allow us to examine the case in which surrounding plates influence the subducting plate, providing a constant driving velocity (kinematically driven collision model), and the case in which surrounding plates have negligible influence on the subducting plate and slab pull is dominant (dynamic collision model).

3 EVOLUTION OF THE REFERENCE MODELS

3.1 Oceanic subduction

We first show the evolution of a model in which a 60-Ma oceanic plate (without attached continent) subducts underneath a continent (model M1, Table 2 and Fig. 3). This provides a reference against which we can test the effects of continental collision. The oceanic and continental domains in our models initially have a same surface elevation of zero. The models need therefore to be run for a few time steps to achieve a regional isostatic surface topography which is determined by the temperature-dependent density and internal strength of the layers. Model M1 achieves a topographic difference

Table 2. List of models.

Model	T_{Moho} (°C)	$T_{\text{lithosphere}}$ (°C)	\bar{v} (cm yr ⁻¹)	$\Delta\rho_{\text{la}}^a$ (kg m ⁻³)	Mantle adiabat (°C km ⁻¹)	UC ^b s_c	LC ^b s_c	LM ^b s_c	Fig.	Remark
M1	586	1300	4	30	0.3	1	1	1	3,4	Oceanic subduction reference
M2	586	1300	4	30	0.3	1	1	1	5,6,8,9,12,15, A1	Continental collision reference
M3	480	1300	4	30	0.3	1	1	1	6,7	
M4	680	1300	4	30	0.3	1	1	1	6,7	
M5	484	1200	1	30	0.3	1	1	1	6,8	
M6	484	1200	4	30	0.3	1	1	1	6,8, A1	
M7	484	1200	8	30	0.3	1	1	1	6,8,15	
M8	586	1300	1	30	0.3	1	1	1	6,8	
M9	586	1300	8	30	0.3	1	1	1	6,8	
M10	685	1400	1	30	0.3	1	1	1	6,8,15	
M11	685	1400	4	30	0.3	1	1	1	6,8, A1	
M12	685	1400	8	30	0.3	1	1	1	6,8	
M13	484	1200	4	30	0.2	1	1	1	A1	
M14	484	1200	4	30	0.4	1	1	1	A1	
M15	586	1300	4	30	0.2	1	1	1	6, A1	
M16	586	1300	4	30	0.4	1	1	1	6, A1	
M17	685	1400	4	30	0.2	1	1	1	A1	
M18	685	1400	4	30	0.4	1	1	1	A1	
M19	586	1300	4	30	0.3	0.1	1	1	9	
M20	586	1300	4	30	0.3	100	1	1	9	
M21	586	1300	4	30	0.3	1	0.001	1	9	
M22	586	1300	4	30	0.3	1	10	1	9	
M23	586	1300	4	30	0.3	1	1	0.1	9	
M24	586	1300	4	30	0.3	1	1	10	9	
M25	586	1300	4	20	0.3	1	1	1	10	
M26	586	1300	4	40	0.3	1	1	1	10	
M27	586	1300	4	30	0.3	1	1	1	10,11,12,15	Dynamic collision model

^aInitial contrast in density between unsubducted oceanic lithosphere and underlying asthenosphere.

^bScaling factor (s_c in eq. 6) for continental upper crust (UC), lower crust (LC) and lithospheric mantle (LM).

between the continental and oceanic domains of about 5 km after *ca.* 20 000 yr. This agrees with the topography difference calculated from Airy isostasy and with general topographic and bathymetric data across passive margins (Turcotte & Schubert 2002). The evolution of surface topography during subduction is shown in Fig. 4. It shows a deep trench with subdued surface topography on the overriding and subducting plates. Subduction of the oceanic slab starts by forming a low viscosity and high strain band within the pre-existing weak seed that helps the oceanic slab to decouple from the continent. The oceanic plate starts to subduct with a dip of about 40° that gradually increases as the slab pull becomes more dominant (Figs 3a–d). The oceanic slab subducts in a bend-backwards mode. This is similar to a subduction mode seen in other numerical and analogue studies (Schellart 2005; Guillaume *et al.* 2009; Li *et al.* 2011; Quinquis *et al.* 2011; van Hunen & Allen 2011). Placed in the context of previous studies that relate slab strength to slab bending behaviour, the bend-backwards mode indicates that our oceanic slab is relatively (but not overly) stiff (Schellart 2008).

3.2 Continent–continent collision

The evolution of the kinematically driven continental collision reference model (M2, set-up in Fig. 2a) is shown in Fig. 5. It shows a transition from initiation of subduction, via a phase of oceanic subduction, to collision. Before collision, the model behaves similar to the oceanic subduction model M1 (compare Figs 3(a)–(c) with 5(a)–(c)). At about 13 Ma, the oceanic slab has completely subducted and collision starts. Model M2 shows a combination of three collision styles: (1) Continental subduction: The upper continental crust is scraped off from the lower crust and accretes at the

trench to produce a high topography of about 5 km (Fig. 5f), but the lower crust subducts together with the lithospheric mantle. Subduction of continental material continues because of the continuous kinematic boundary condition at the right-hand side of the model domain. The topography increases, but never reaches values higher than 5 km (Fig. 5f). (2) Folding: The right continent shows the onset of large-wavelength (~300 km), low-amplitude (~0.1 km) folding as shown in Figs 5(d)–(f). Folding appears in the model 9 Myr after initiation of continental collision and progressively increases in time, but remains of low amplitude. (3) Thickening: Continental thickening is accommodated by off-scraping of the upper continental crust at the trench and formation of a frontal accretionary wedge (Fig. 5e). The accretionary wedge grows during the collision phase. Sediments and crustal material that are not off-scraped subduct to subcrustal depths. Our kinematically driven collision models do not show evidence of exhumation of high pressure rocks.

Our results are consistent with previous studies (Pysklywec *et al.* 2000; Toussaint *et al.* 2004a; Burov & Yamato 2008; Selzer *et al.* 2008), which found that a fast driving velocity (>3–5 cm yr⁻¹), a weak lower continental crust and cold to moderate Moho temperatures (<600 °C) can result in a combination of stable subduction, lithospheric-scale folding and thickening, but that stable subduction will be the dominant style of deformation for these systems.

4 CONTROLS ON COLLISION STYLES

4.1 The influence of driving velocity and temperature

Previous studies have shown that driving velocity and temperature are two primary factors which can control the style of collision

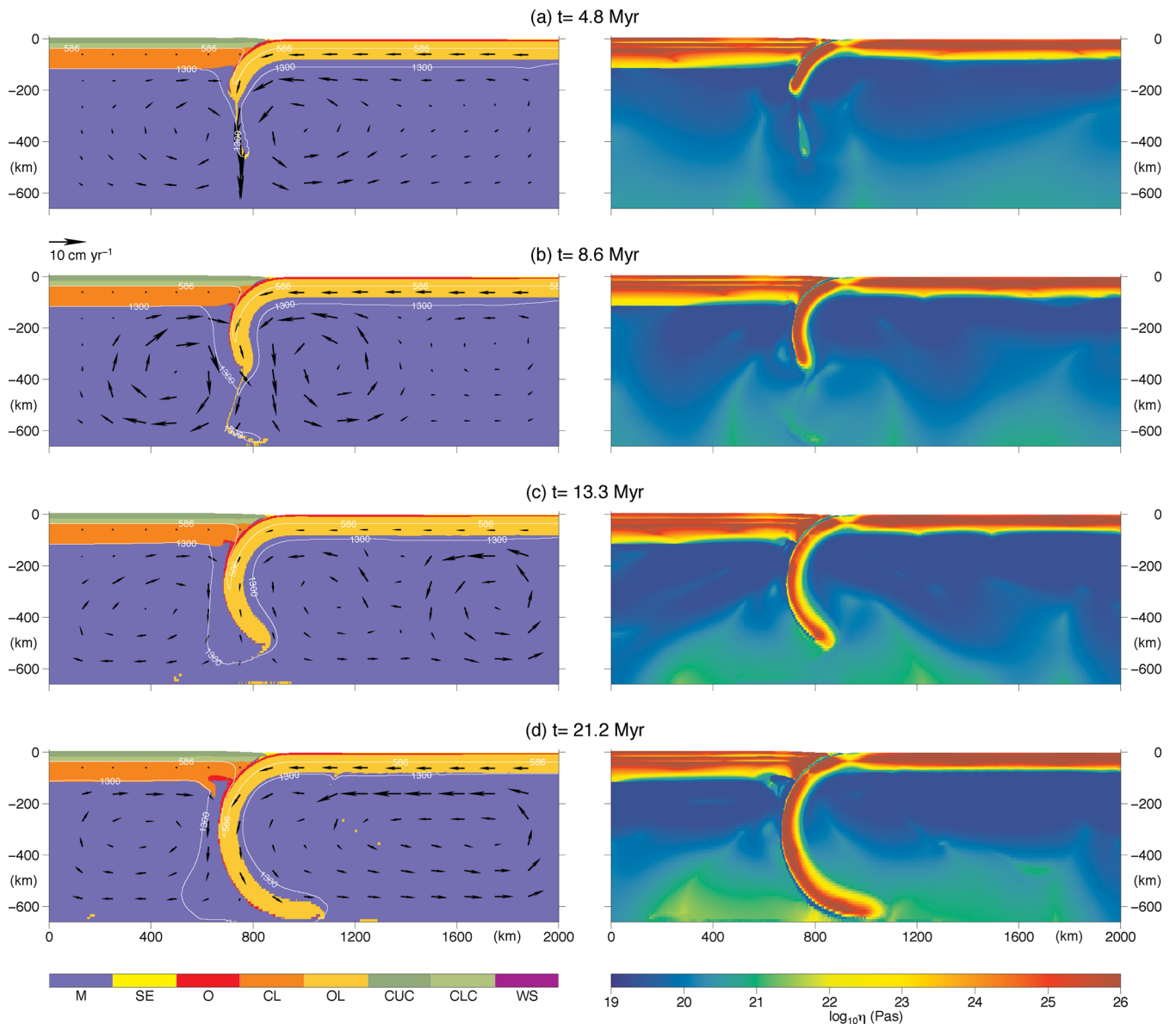


Figure 3. Evolution of the reference model M1 (see Table 2) in which a 60-Ma oceanic plate subducts under a continent (no continental collision). Material properties (left-hand panels) and logarithmic viscosity snapshots (right-hand panels) after (a) 4.8, (b) 8.6, (c) 13.3 and (d) 21.2 Myr. The two isotherms show 586 and 1300 °C, representing the temperature at the Moho and base of the continental lithosphere in the initial state, respectively.

(Pysklywec *et al.* 2000; Toussaint *et al.* 2004a; Burov & Yamato 2008). Toussaint *et al.* (2004a,b) investigated the effect of continental temperature using models with an initial Moho temperature which was varied between 400 and 1000 °C, whereas the surface temperature was kept at 0 °C. Their models have 1330 °C at the base of the asthenosphere at 250 km depth, and 2200 °C at 660 km depth. This implies a hot mantle with an adiabat of 2.12 °C km⁻¹, which is about one order of magnitude larger than the expected adiabat of the mantle (Turcotte & Schubert 2002). Because temperatures of lithological layers cannot be varied individually, but are linked through the geothermal gradient, not only crustal temperature is varied, but also the temperature of the lithospheric mantle. It is therefore an open question whether the different styles of the models are caused by changes in crustal temperature, changes in lithospheric temperature, or both.

To investigate the roles of crustal and lithospheric mantle temperature, we first set up cold (M3) and warm (M4) continental crust

models using the thermal parameters of Table 3 (see also Table 2). The initial Moho temperature for our cold and warm models is 480 and 680 °C, respectively (our reference model M2 has a Moho temperature of 586 °C). Surface temperature is 0 °C, and temperature at the base of the continental lithosphere is 1300 °C (Fig. 6a). Our models also differ in lithospheric temperature, but the largest temperature difference occurs at the Moho. They have the same sublithospheric mantle temperature which follows a 0.3 °C km⁻¹ mantle adiabat. Models M3 and M4 give the largest variation in Moho temperature that can be achieved within a realistic range of thermal parameters. Our Moho temperature variation is less than in Toussaint *et al.* (2004a). Fig. 7 shows that the effect of Moho temperature on the style of continental collision is essentially small over the range of temperatures we investigated. The models show stable continental subduction and the formation of an accretionary wedge at the trench. The warmer (and therefore rheologically weaker) crust model cannot sustain the high topography of the colder (stronger)

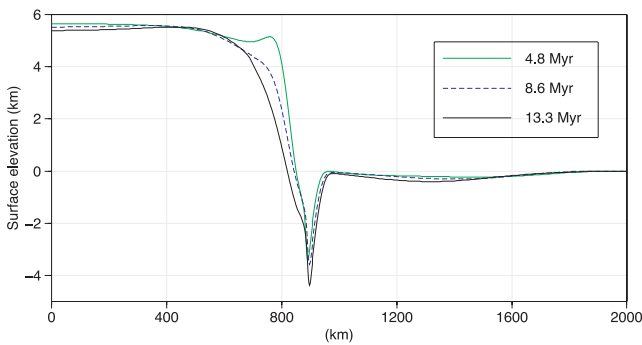


Figure 4. Surface topography evolution of the continent–ocean reference model (M1) after 4.8, 8.6 and 13.3 Myr.

model (Fig. 7). This can be understood as the response of an accretionary wedge building above a weak base. For low basal dip angles, a reduction in basal strength leads to a reduction in topography (Davies & Engelder 1985; Huiqi *et al.* 1992; Buiter 2012). Our results indicate that different styles of collision are probably not only caused by variations in the temperature of the Moho (within reasonable thermal values) and that other parameters may play a role.

We therefore next investigate the role of crustal and mantle temperature by varying the initial geotherm from a cool geotherm, with $T_{lc} = 1200$ °C at the base of the continental lithosphere and $T_{lo} = 1188$ °C at the base of the oceanic lithosphere (models M5–M7), to a warm geotherm with $T_{lc} = 1400$ °C and $T_{lo} = 1388$ °C (models M10–M12) (Fig. 6b). The largest temperature difference between these models occurs in the lithospheric and sublithospheric mantle. For these models, we also examine the role of driving velocity by varying the velocity of the incoming plate between 1 and 8 cm yr⁻¹ (Table 2). Fig. 8 shows the models after 24 Myr of convergence in temperature–velocity space. The models show almost all collision mechanisms: stable subduction, thickening, folding and lithospheric dripping. Slab break-off does not occur because the combination of the continuous push applied by the driving boundary velocity with slab pull overcomes the upward buoyancy of the subducted continental materials, for our model set-up and parameter values. Fig. 8 allows us to deduce the following trends:

(1) Stable continental subduction occurs over a wide range of temperatures ($T_{lc} = 1200$ – 1400 °C) and velocities (between 1 and 8 cm yr⁻¹).

(2) Lithospheric folding plays a role only in cool systems ($T_{lc} \approx 1200$ °C, $T_{Moho} = 484$ – 685 °C) at high driving velocities (above 4 cm yr⁻¹).

(3) RT-type of dripping of continental lithosphere is seen only in hot systems ($T_{lc} \gtrsim 1350$ °C). RT-dripping is more effective at low driving velocities, as the lower velocity implies a lower viscous strength of the continental lithosphere.

(4) Lithospheric thickening occurs by two mechanisms: First, thickening in the trench region associated with off-scraping of the crust and accumulation of crustal material at the trench occurs in all models of continental subduction. Secondly, thickening of the continents accommodated by pure shear occurs in models with a hot geotherm ($T_{lc} = 1350$ °C).

These models illustrate that crust and mantle temperature (rather than Moho temperature alone) and driving velocity play crucial roles in determining continental collision styles. Since both lithospheric and mantle temperature change from a cold to a hot geotherm in our models (see Fig. 6b), it is an open question whether lithospheric

temperature or mantle temperature is the primary factor. To address this question, we varied mantle temperature for a fixed lithospheric temperature (Fig. 6c). Mantle temperature changes from cold (mantle adiabat = 0.2 °C km⁻¹), via intermediate (mantle adiabat = 0.3 °C km⁻¹), to hot (mantle adiabat = 0.4 °C km⁻¹) for a cold (M6), intermediate (M2) and hot (M11) lithosphere model (resulting in six extra models, Fig. A1). We find that sublithospheric thermal variations in a realistic range do not effect the style of collision for a cold and intermediate temperature lithosphere on the timescale of our models. An increase in the mantle temperature for a warm lithosphere ($T_{lc} = 1400$ °C) facilitates RT-type dripping, because the warm mantle further warms up the continental lithosphere, inducing additional weakening of the lithosphere from the base (we come back to this in the Discussion). Based on our model results, we can therefore conclude that lithospheric temperature (rather than crustal or mantle temperature alone) constitutes an important control on collision style.

4.2 The influence of continental rheology

Temperature variations imply only a limited strength variation (within realistic values for thermal parameters) and it is difficult to vary crustal and mantle temperature separately. We therefore here investigate a wider range of variations in continental strength by varying the rheological stratification of the continents in the kinematically driven collision model (Fig. 9). The driving velocity is again 4 cm yr⁻¹ and T_{lc} is 1300 °C. The rheological strength of the continental upper crust, lower crust and lithospheric mantle is varied by multiplying the viscosity with a factor s_c following eq. (6) (Table 2). The rheology of each continental layer is changed separately, keeping the other two layers the same as in the reference model. The strength of the oceanic lithosphere is the same for all these models.

The upper crust is scraped off from the lower crust and accumulated at the trench to form an accretionary wedge for models with an upper crust of moderate-to-weak strength (models M2 and M19). An increase in upper crustal strength (model M20) facilitates subduction of the entire continental crust to lithospheric depths. Continents with a strong upper crust are also more likely to experience folding during collision (model M20). Our results show that in the case of a weak lower crust (model M21), the entire continental crust decouples from the subducting lithospheric mantle and accumulates at the trench. This increases crustal thickening, but stable subduction remains the dominant style of deformation. Weakening of the continental lithospheric mantle (model M23) promotes pure shear-type of thickening and RT-type of lithospheric dripping, whereas stable subduction occurs for stronger lithospheres (models M2 and M24). Our variations in continental strength are large (Fig. 9b) and could in nature only be achieved by lithological differences or localized weakening mechanisms, as changes in temperature or velocity would not effect individual layers only. The strength of the upper and lower crust controls continental crust subductability, whereas the strength of the lithospheric mantle controls lithospheric thickening, RT-style dripping and subduction of the continental lithosphere.

4.3 The influence of adjacent plates

Our models so far all examined kinematically driven collision (Fig. 2a), in which convergence across the interplate contact is maintained by a driving velocity which simulates a combination of a push by adjacent plates and ridge push. We investigate the role of

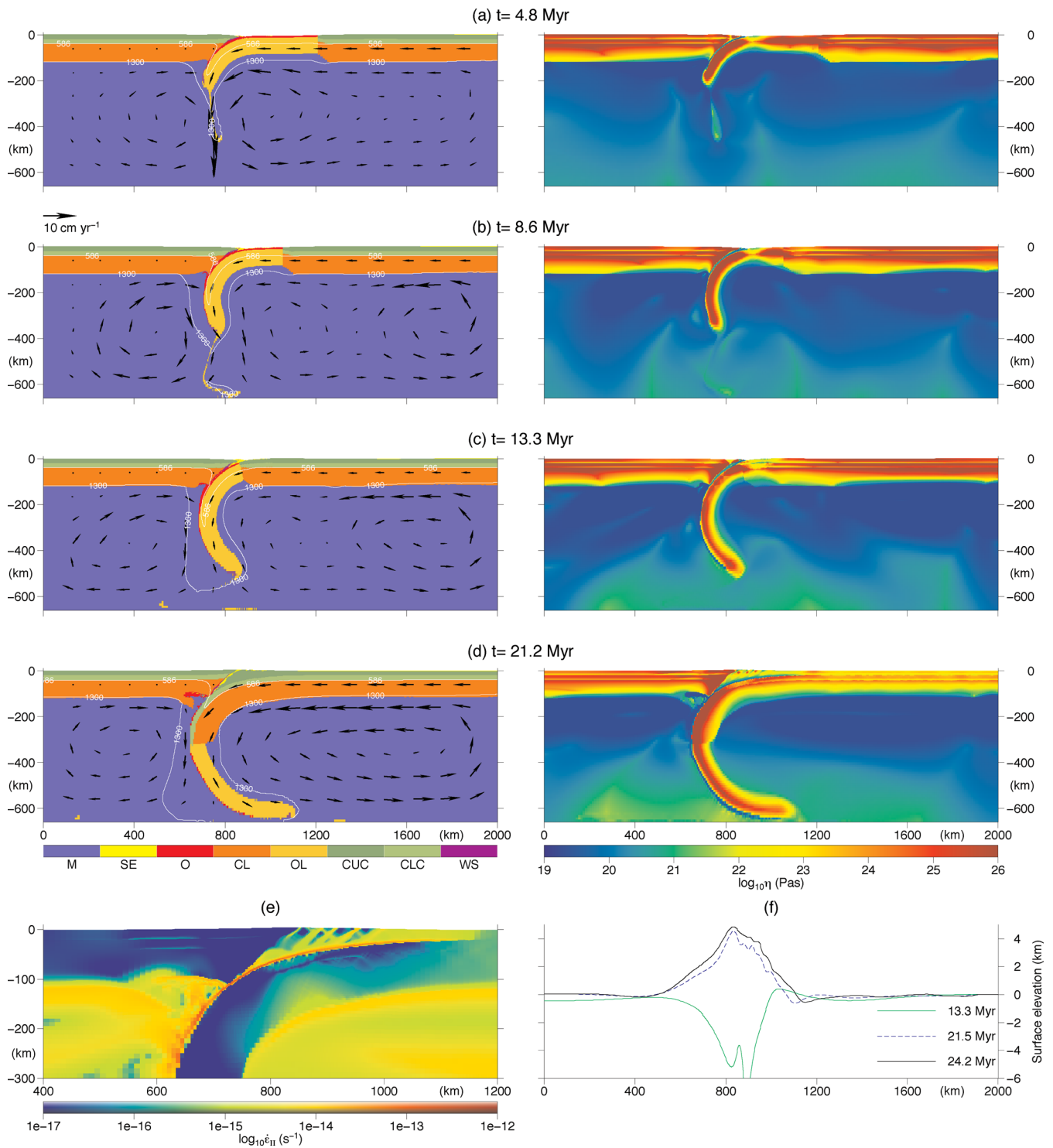


Figure 5. Evolution of the continental collision reference model (M2, Fig. 2a). Material properties (left-hand panels) and viscosity snapshots (right-hand panels) after (a) 4.8, (b) 8.6, (c) 13.3 and (d) 21.2 Myr. Two isotherms show 586 and 1300 °C, representing the temperature at Moho and base of the continental lithosphere in the initial state, respectively. (e) Logarithmic strain-rate $\log_{10}(\dot{\epsilon}_{II})$ after 24.2 Myr showing formation of an accretionary wedge at upper crustal depths. The wedge forms close to the trench and dominantly develops forward thrusts towards the right. (f) Surface topography showing the onset of lithospheric-scale folding of the incoming continent and formation of high topography at the trench.

adjacent plates with a dynamic collision set-up (Fig. 2c), in which the kinematic boundary condition is removed once the system is self-sustaining. The first steps of the dynamic collision model are similar to the kinematically driven model (Figs. 5 and 10). We initiate subduction and drive the rightmost continent towards the trench

by applying a driving velocity of 4 cm yr^{-1} . After 7 Myr, we remove the imposed velocity, leaving the model to develop internally. The production of new continental material at $x = 1800 \text{ km}$ also ceases at this stage. Since the rightmost continent is decoupled from the side boundary, the continent is now more free to move in response

Table 3. Thermal parameters of cold (M3), intermediate (M2) and warm (M4) crust models.

	Upper crust		Lower crust		Lithospheric mantle	
	k	Q	k	Q	k	Q
Cold	2.5	6e-8	2.5	1e-7	2.6	4e-8
Intermediate	2.5	0.58e-6	2.5	0.58e-6	2.8	0.0
Warm	2.5	1.4e-6	2.5	6e-7	3.3	2e-8

Note: k is thermal conductivity ($\text{W m}^{-1} \text{K}^{-1}$) and Q is volumetric heat production (W m^{-3}).

to the competition between slab pull, mantle resistance and positive buoyancy of subducted continental material.

Subduction of the oceanic slab continues until the whole slab is subducted and the continent starts to subduct (Fig. 10b). From

this stage on, the convergence velocity between the two continents decreases owing to the increased resistance to subduction caused by the subducting positively buoyant continental material (Fig. 11a). The competition between slab pull and positive buoyancy of the subducting continent leads to an extensional regime in the subducted slab, finally resulting in necking and slab break-off similar to, for example, Andrews & Billen (2007) and Duretz *et al.* (2012) (Fig. 10c). Our dynamic collision reference model experiences a deep slab break-off (280 km depth) at about 18 Myr after initiation of collision. Slab break-off is accompanied by rapid surface uplift at a rate of *ca.* 0.6 km Myr^{-1} , which is in the range of post break-off uplift rates found in previous studies (Andrews & Billen 2007; Duretz *et al.* 2011). Maximum surface topography reaches about 4.2 km at *ca.* 2 Myr after break-off, which is similar to break-off related uplift found in previous studies (Buiter *et al.* 2002; Baumann *et al.* 2010;

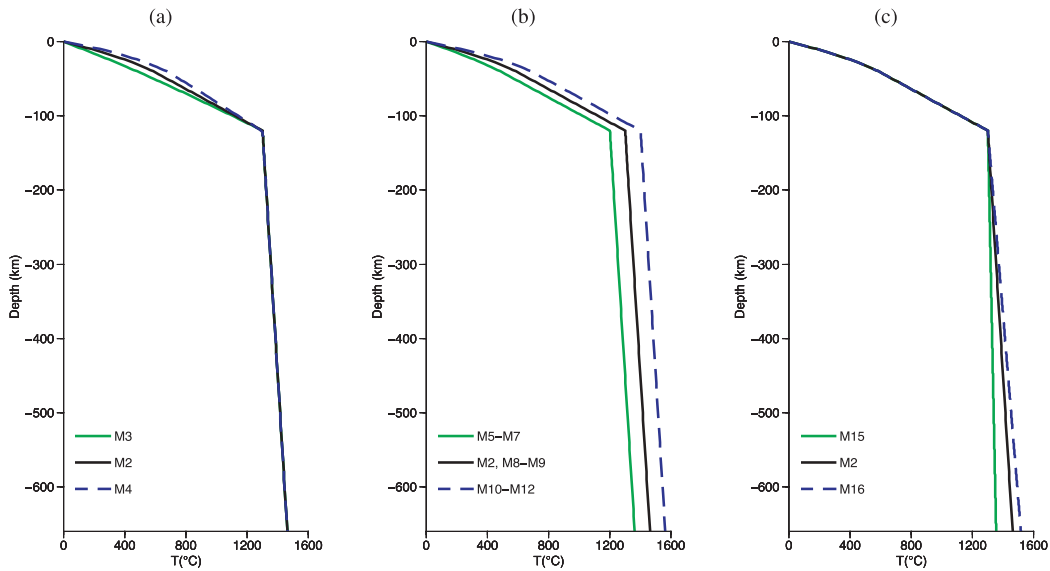


Figure 6. Initial thermal structure of the continents for models M2–M12 that examine the effects of variations in crustal and lithospheric temperature. (a) Thermal structure for model M3 with a cold crust ($T_{\text{Moho}} = 480 \text{ }^\circ\text{C}$), reference model M2 with an intermediate temperature crust ($T_{\text{Moho}} = 586 \text{ }^\circ\text{C}$) and model M4 with a hot crust ($T_{\text{Moho}} = 680 \text{ }^\circ\text{C}$). Temperature is fixed at $1300 \text{ }^\circ\text{C}$ at the base of the lithosphere (at 120 km depth). (b) Thermal structure for models M2 and M5–12 in which temperature is varied in the entire lithosphere and mantle, from a cold lithosphere ($T_{\text{lc}} = 1200 \text{ }^\circ\text{C}$, M5–7), through an intermediate lithosphere ($T_{\text{lc}} = 1300 \text{ }^\circ\text{C}$, M2 and M8–9), to a hot lithosphere ($T_{\text{lc}} = 1400 \text{ }^\circ\text{C}$, M10–12). (c) Thermal structure for models with an intermediate temperature crust and lithosphere (as in M2), intermediate (M2) and cold (M15) and hot (M16) mantle.

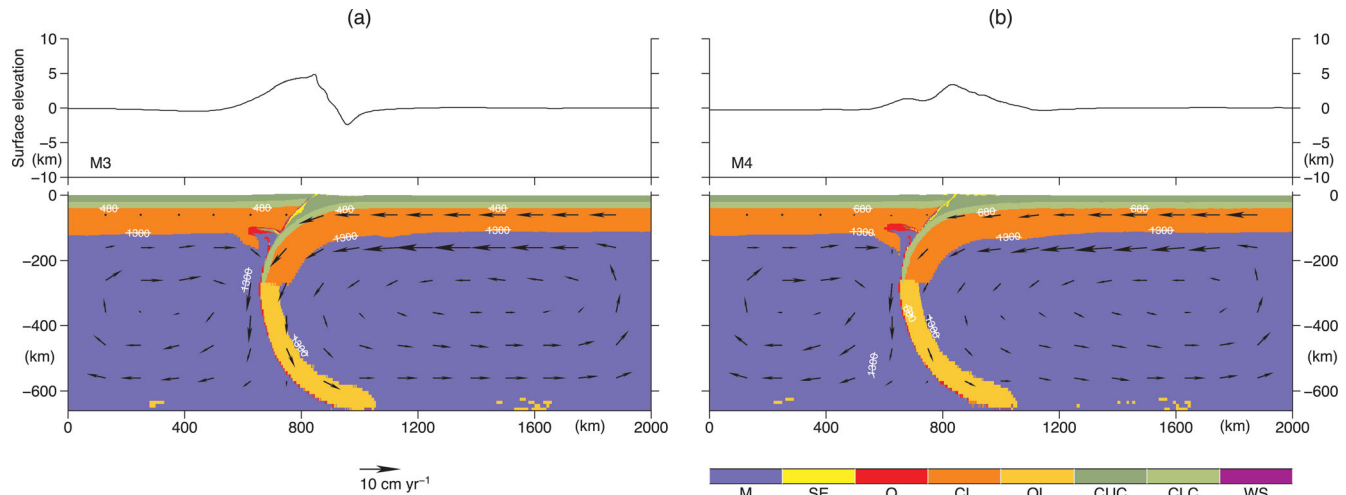


Figure 7. Effect of Moho temperature on continental collision in the kinematically driven collision model (see also Fig. 6a). Results after 20 Myr of convergence. (a) Cold crust model (M3) with a Moho temperature of $480 \text{ }^\circ\text{C}$. (b) Hot crust model (M4) with a Moho temperature of $680 \text{ }^\circ\text{C}$. Both models show essentially the same style of deformation, but the warmer (weaker) crust model builds less topography.

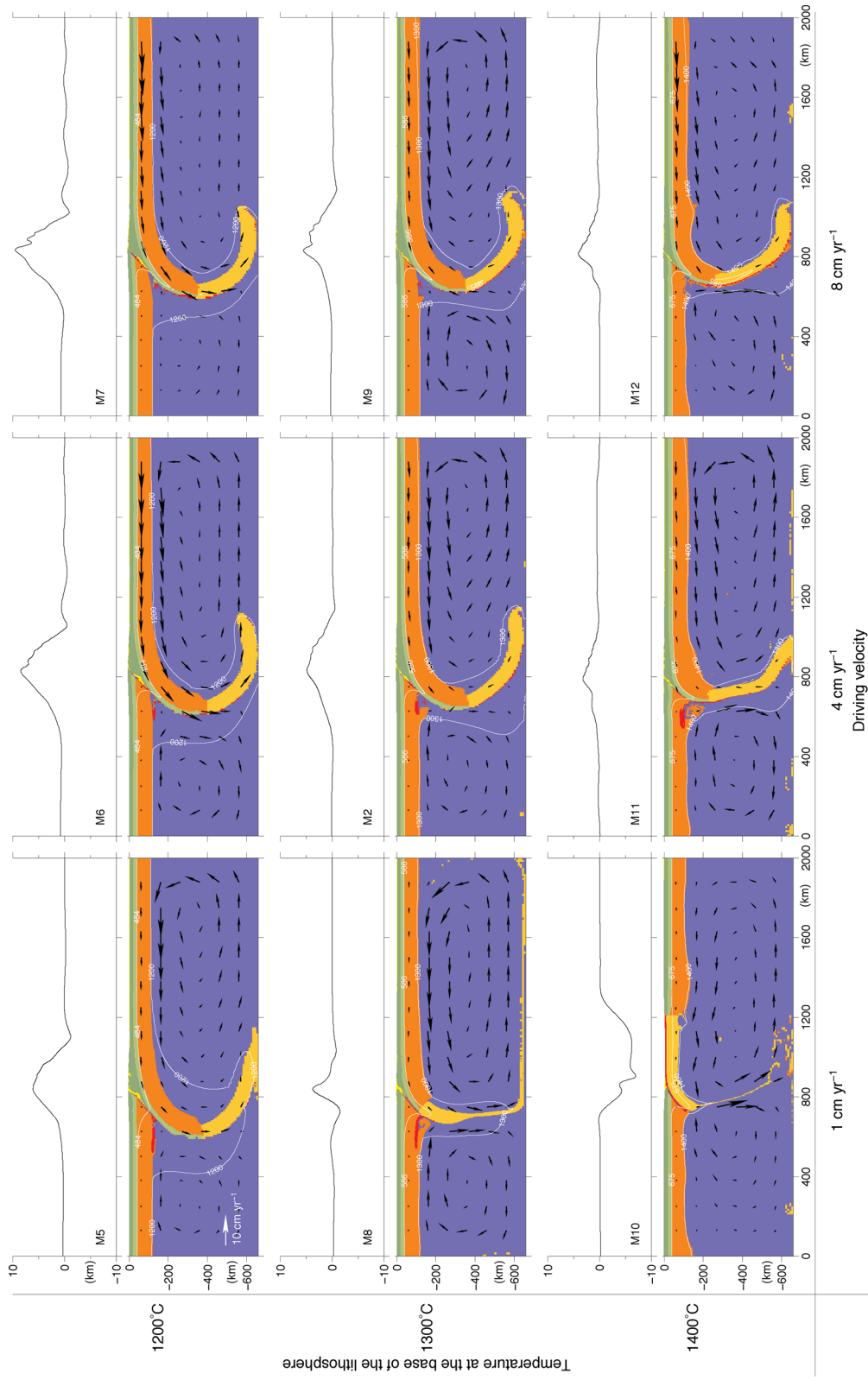


Figure 8. Influence of continental temperature, as characterized by the temperature at the base of the lithosphere (Fig. 6b), and driving velocity on the kinematically driven collision model. Results show material and velocity fields after 24 Myr of convergence, with surface topography at the top of each panel.

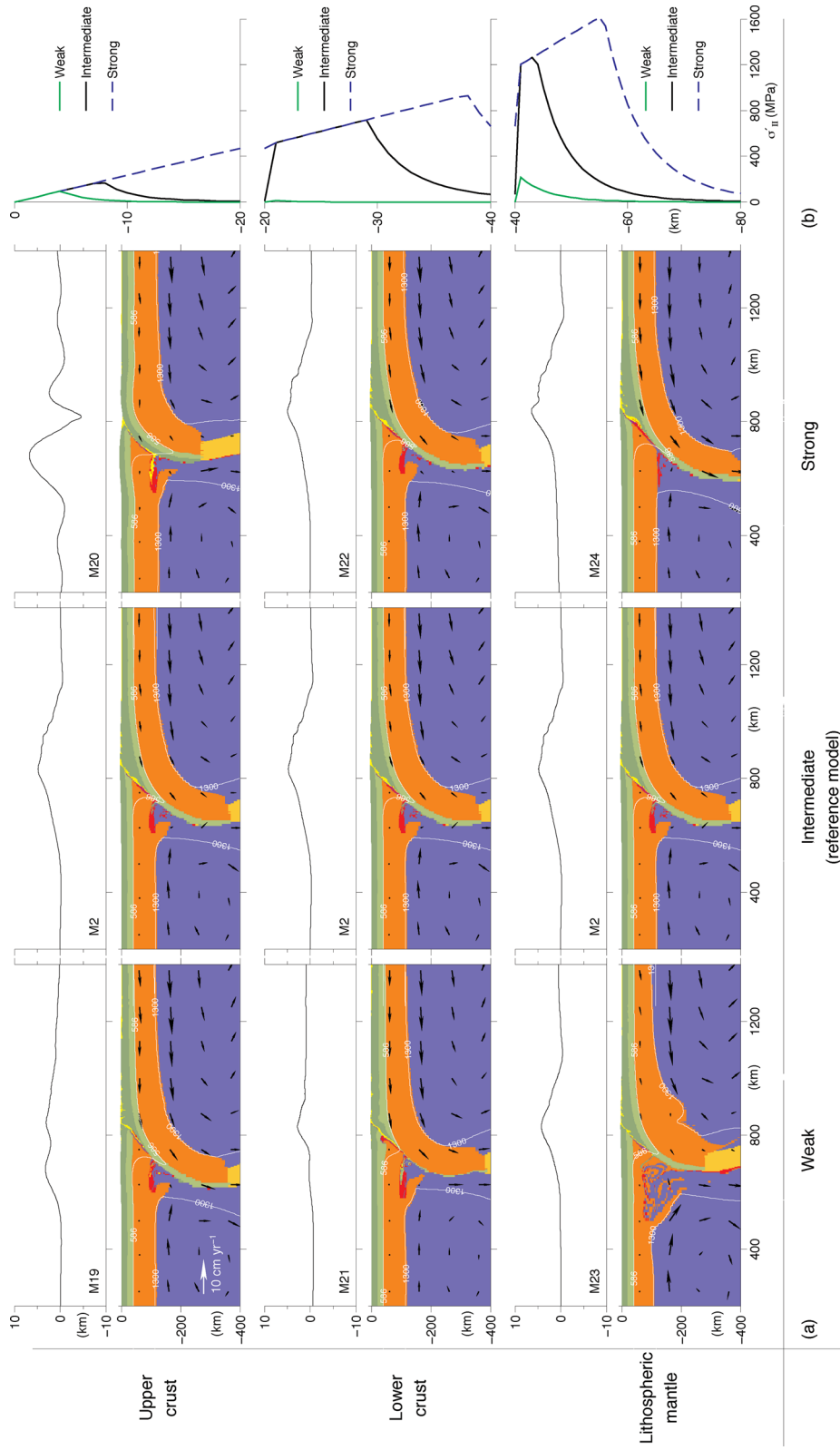


Figure 9. (a) Kinematically driven collision models after 24 Myr convergence showing the effects of variations in strength of the continental crust and lithospheric mantle. Strength variations are obtained by multiplying the viscous flow laws with a scaling factor (s_c in eq. 6, see also Table 2). Variations in strength of the upper crust in the top row, lower crust in the middle row and lithospheric mantle in the bottom row. Left column weak case, middle column intermediate case and right column strong case. Surface topography is shown at the top of each panel. (b) Initial continental effective stress profiles.

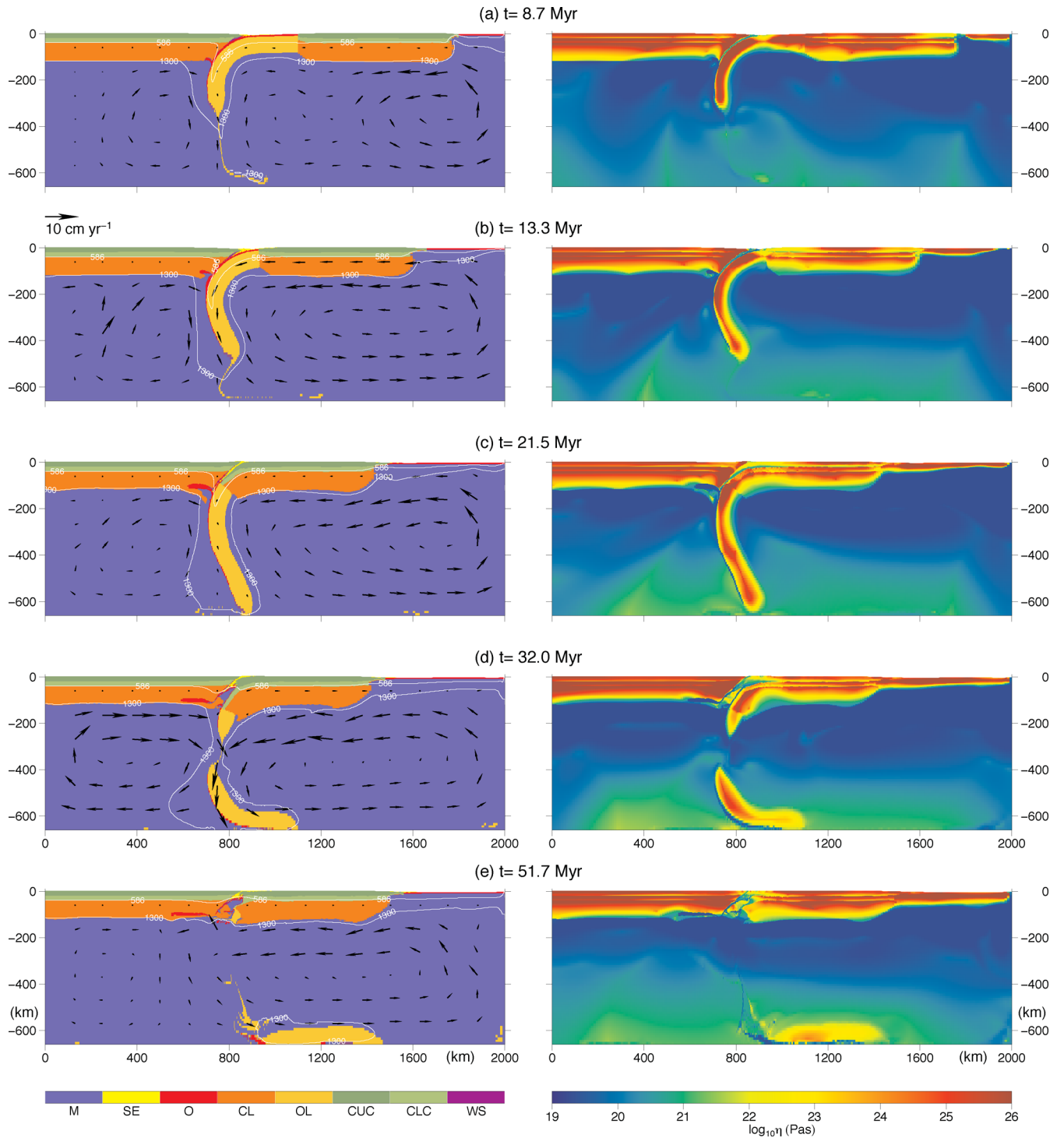


Figure 10. Evolution of the dynamic continental collision model (M27, Fig. 2c). Material properties (left-hand panels) and logarithmic viscosity snapshots (right-hand panels) after (a) 8.7, (b) 13.3, (c) 21.5, (d) 32.0 and (e) 51.7 Myr. The right continent is driven with $v = 4 \text{ cm yr}^{-1}$ until $t = 7 \text{ Myr}$, after which the driving velocity is removed and slab pull is the only driving force in the model. The two isotherms at 586 and 1300 °C represent the temperature at the Moho and base of the continental lithosphere in the initial state, respectively.

Duret *et al.* 2011). Maximum topography is therefore similar in the kinematically driven (M2) and dynamic (M27) collision models (Figs 5f and 11b), but the mechanisms creating surface uplift are different: The kinematically driven collision model creates a long-term topography through accretionary wedge formation and the maximum topography increases with time (Fig. 12). In contrast,

topography in the dynamic collision model is supported dynamically and increases after break-off before slowly reducing to *ca.* 2 km over a long period of time ($\sim 24 \text{ Myr}$, Fig. 12). The topography reduction occurs when the formerly subducting slab experiences about 90 km of reverse motion termed ‘eduction’ (Andersen *et al.* 1991, measured horizontally along the surface) (Figs 11b and 12).

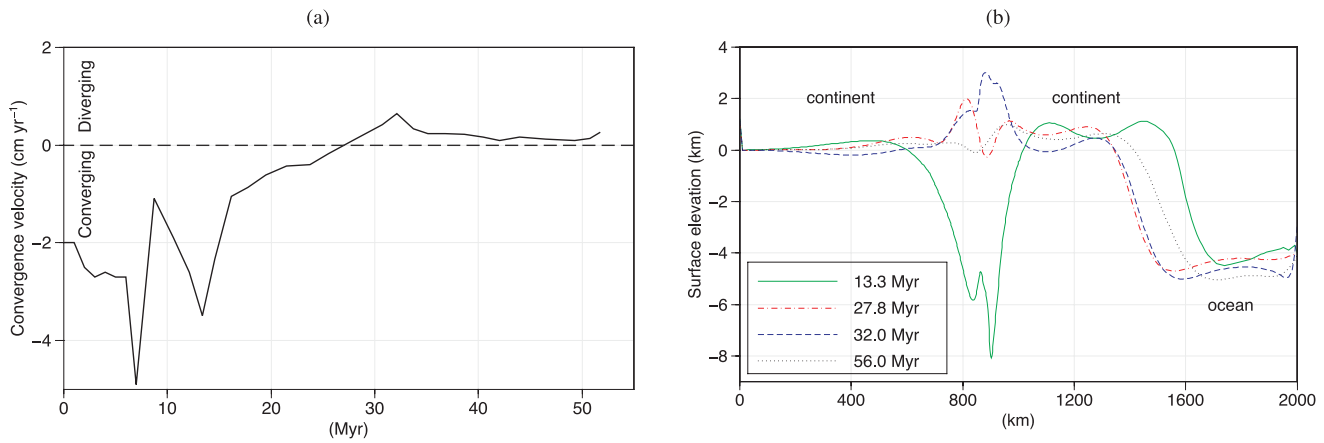


Figure 11. (a) Relative velocity between the two continents of the dynamic collision model (M27) plotted versus time. (b) Surface topography of the dynamic collision model (M27) in the oceanic subduction (13.3 Myr), necking (27.8 Myr), break-off (32.0 Myr) and reverse motion (56.0 Myr) phases.

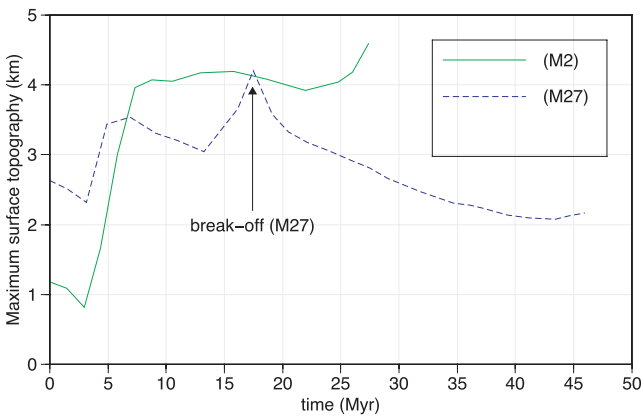


Figure 12. Maximum surface topography of the kinematically driven collision model (M2) and the dynamic collision model (M27) versus time. Time axis is measured from the initiation of continental collision, when the entire intervening ocean has been subducted.

This amount of reverse motion is smaller in magnitude than the exhumation of 180 km that Andersen *et al.* (1991) determined for the Norwegian Caledonides.

Exhumation of subducted continental crust and sediments is triggered before slab break-off by opening of a subduction channel due to slab retreat and upward buoyancy flow of crustal material and sediments in the opened channel. Although exhumation initiates before break-off, most exhumation occurs after break-off when the model experiences reverse motion. Subducted materials experience peak pressures of *ca.* 2.5 GPa and temperatures of *ca.* 580 °C before exhumation, which is in the range of natural peak pressure and temperature of UHP rocks reported by previous workers (Andersen *et al.* 1991; Jamtveit *et al.* 1991; Hacker 2006; Hacker *et al.* 2010). It has been suggested that confinement of weaker rocks in a constrained flow between strong materials (the so-called high-pressure cooker) could lead to non-lithostatic pressure of up to 1–2 GPa (Mancktelow 2008; Li *et al.* 2010; Vrijmoed *et al.* 2009). This would imply that UHP conditions are reached at shallower depth than in a lithostatic pressure environment. The development of dynamic pressure depends on the crustal and mantle rheology and convergence velocity of the plates (Mancktelow 2008; Li *et al.* 2010). Our dynamic collision reference model does not show significant non-lithostatic pressure (order of few MPa in magnitude) and UHP rocks in our models record therefore lithostatic pressure. Our

models show that collision systems could experience a relatively large control by their surrounding plates. Forced convergence can cause deep subduction of continental material. Less control by adjacent plates can lead to exhumation of deep subducted rocks and slab break-off.

4.4 The influence of the density of the oceanic lithosphere

Many subduction models impose an initial contrast in density between the unsubducted oceanic lithosphere and the underlying asthenosphere. This density contrast is modified during model evolution as the subducted slab warms up (eq. 5). The density difference determines slab pull and changes in its value can therefore effect the dynamics of subduction and collision. Previous numerical studies have used values for the initial density difference between oceanic lithospheric mantle and asthenosphere $\Delta\rho_{la}$ between 0 and 50 kg m⁻³ (e.g. Toussaint *et al.* 2004a; Babeyko & Sobolev 2008; Warren *et al.* 2008). Afonso *et al.* (2007) pointed out that the density difference probably does not exceed 40 kg m⁻³. We examine the effect of variations in $\Delta\rho_{la}$ of 20, 30 and 40 kg m⁻³ by changing the initial density of the oceanic lithospheric mantle from 3270 to 3290 kg m⁻³. This implies a variation from a weak to a strong slab pull. Our reference models (M2, M27) have a $\Delta\rho_{la}$ of 30 kg m⁻³. Our dynamic collision model is not sensitive to density variations of ± 10 kg m⁻³. Dynamic collision with strong, moderate, and weak slab pull (20, 30, and 40 kg m⁻³ density contrast) show the same collision style, with break-off being the dominant style of deformation. Results from our kinematically driven models with the same differences in density contrast also indicate that this order of variation is not powerful enough to make notable changes in the style of collision (Fig. 13).

5 DISCUSSION

We have shown how lithospheric temperature and driving velocity change the deformation style in kinematically driven collision systems (Fig. 8) from RT-dripping at high temperatures ($T_c \gtrsim 1350$ °C), via stable subduction for moderate to high temperatures (1250 °C $\lesssim T_c \lesssim 1350$ °C) and for a wide range of driving velocities ($1 \lesssim V_{dv} \lesssim 8$ cm yr⁻¹), to folding at low temperatures ($T_c \approx 1200$ °C) and high velocities ($V_{dv} \gtrsim 6$ cm yr⁻¹). Our results are consistent with previous studies (Pysklywec *et al.* 2000; Toussaint *et al.* 2004a; Burov & Yamato 2008), except that the

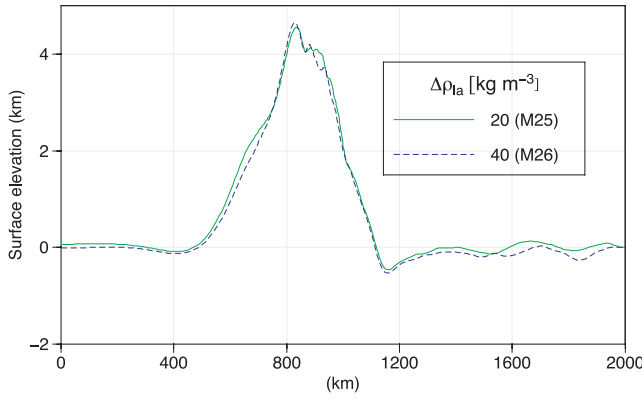


Figure 13. Surface topography after 24 Myr convergence for the kinematically driven collision model with an initial density difference $\Delta\rho_{la}$ between oceanic lithosphere and sublithospheric mantle of 20 and 40 kg m^{-3} (the reference model uses $\Delta\rho_{la} = 30 \text{ kg m}^{-3}$).

boundaries in temperature–velocity space between the different collision styles are somewhat shifted. For example, our models show that folding is likely to occur at the same or cooler geotherm for which stable subduction occurs, whereas previous studies (Toussaint *et al.* 2004a; Burov & Yamato 2008) have suggested that folding can also happen in hotter systems. Part of the differences between our study and previous studies is to be expected since differences occur in rheology, density, softening mechanisms and model set-up.

We have illustrated how the collision mechanisms depend on the continental rheological stratification and the initial density contrast between oceanic lithospheric mantle and the asthenosphere. We found that an increase in strength of the upper continental crust facilitates subduction of the entire crust to lithospheric depths (Fig. 9). An upper crust of moderate-to-weak strength is more likely to be scraped-off at the trench and contribute to the formation of an accretionary wedge. Accretion of the entire crust is feasible when the lower crust is weak. An intermediate-to-strong lithospheric mantle leads to subduction, but weakening of the continental lithospheric mantle leads to RT-type of dripping. We found that changes in the initial density contrast between the oceanic lithospheric mantle and underlying mantle on the order of 20 kg m^{-3} do not cause notable differences in the style of kinematically driven collision models (Fig. 13).

The transition between lithospheric folding and thickening can be predicted by considering the Ar number, which is given as the ratio of stress caused by gravity to stress caused by shortening (Schmalholz *et al.* 2002)

$$Ar = \frac{\Delta\rho g H}{2\eta_{\text{eff}}\dot{\epsilon}_{\text{bg}}}, \quad (10)$$

where $\Delta\rho$ is the density contrast between lithosphere and asthenosphere, H and η_{eff} thickness and effective viscosity of lithosphere and $\dot{\epsilon}_{\text{bg}}$ background strain-rate. Following Schmalholz *et al.* (2002), folding would dominate over lithospheric thickening if $Ar < 2.5n$ (using a thick-plate solution). Acknowledging the simplifications inherent in this equation and the values of its parameters, we find that our models can exhibit folding or thickening, with a tendency towards folding.

To understand the roles of velocity, temperature, rheology and density, we look at the forces in a collision system (Fig. 14). The slab pull force can be calculated from the density contrast ($\Delta\rho_s$)

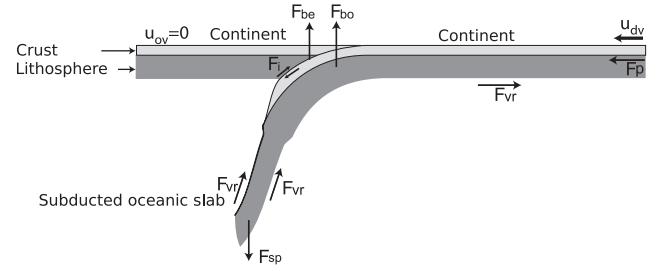


Figure 14. Cartoon illustrating the forces in a continent–continent collision system. F_p , push force; F_{vr} , viscous resistance force; F_{bo} , buoyancy force; F_{be} , bending force; F_{sp} , slab pull force; F_i , shear resistance on interplate contact; u_{dv} , driving velocity and u_{ov} , overriding continent velocity.

between subducted oceanic lithosphere and surrounding mantle and the length (L_s) of the subducted slab (Turcotte & Schubert 2002):

$$F_{sp} \simeq \Delta\rho_s g L_s h, \quad (11)$$

where h is the thickness of the slab. In our models, F_{sp} is on the order of $2 \times 10^{13} \text{ N m}^{-1}$ for the oceanic subduction phase. This is consistent with previous studies and analytical calculations that found a slab pull in the range of $1\text{--}5 \times 10^{13} \text{ N m}^{-1}$ (Molnar & Gray 1979; Bott *et al.* 1982; Davies & von Blanckenburg 1995; Turcotte & Schubert 2002; Funicello *et al.* 2003). We computed the density difference $\Delta\rho_s$ over the entire subducted lithosphere, including crustal material. Slab pull changes with variations in crustal and lithospheric temperature, as in models M3 and M4 (Fig. 6a) and for variations in mantle temperature only (models M15 and M16, Fig. 6c). However, models in which lithospheric temperature is changed but the temperature at the base of the lithosphere and mantle are shifted by the same amount (models M5–M7 and M10–M12, Fig. 6b) have little impact on slab pull, because the relative temperature difference between the slab and surrounding mantle stays approximately the same. The push force F_p simulates the interaction of the continental plate with adjacent plates in natural settings in a simplified manner and can be calculated from

$$F_p \simeq \int_0^{h_{cl}} \sigma_{xx} dy, \quad (12)$$

where h_{cl} is the continental lithospheric thickness and σ_{xx} the stress component in the horizontal direction. In our dynamic collision models, the right continent is decoupled from the side boundary and can move more freely in response to slab pull. Only a small ‘ridge push’ from our simulated ridge acts on the right continent in this case. In kinematically driven collision models, the right continent is pushed with a constant velocity, which does not imply a constant stress or push force. Therefore, the push force differs most between our kinematically driven ($1\text{--}7 \times 10^{12} \text{ N m}^{-1}$ towards the trench) and dynamic ($2\text{--}8 \times 10^{11} \text{ N m}^{-1}$ away from the trench) collision models after initiation of continental collision. Our push force magnitudes are within the range of push forces on the order of $1\text{--}7 \times 10^{12} \text{ N m}^{-1}$ found in previous studies (Parsons & Richter 1980; Toth & Gurnis 1998; Turcotte & Schubert 2002; Funicello *et al.* 2003). The primary resisting force to subduction is the slab bending force (F_{be}). For viscous plates, this force can be calculated from (Turcotte & Schubert 2002)

$$F_{be} \simeq -\frac{u_{\text{conv}} h^3 \eta_s}{r^3}, \quad (13)$$

where η_s is the slab effective viscosity, r slab curvature at the trench and u_{conv} is convergence velocity. The minus sign indicates that this force is a resistive force against subduction. The numerical

value for r is obtained by fitting the best circle that accommodate top interface of the subducted slab and separate it from overriding continent and its surrounding mantle. In our models, this force is on the order of $3 \times 10^{12} \text{ N m}^{-1}$ for the oceanic subduction phase, which is of the same order of magnitude as found by Buffett & Becker (2012). The continental collision phase leads to a bending force which is one order of magnitude smaller. The convergence velocity u_{conv} directly changes F_{be} , but temperature variations also play a role through their effect on the effective viscosity of the slab. The viscous mantle resistance force (F_{vr}) acts on the top and bottom of the subducted slab and at the base of the continental plate (mantle drag). It can be calculated from the viscosity of the mantle (η_m) and the mean velocity of the incoming continent (u_{dv}) (Turcotte & Schubert 2002)

$$F_{\text{vr}} \simeq -\eta_m u_{\text{dv}}. \quad (14)$$

This force can affect our model styles when changes occur in mantle rheology, temperature or convergence rate. The range of this force in our models is from 3×10^{10} to $1 \times 10^{11} \text{ N m}^{-1}$. This is of similar order of magnitude as obtained from simple calculations assuming an upper-mantle viscosity of 10^{19} – 10^{21} Pa s (e.g. Steinberger & Calderwood 2006; Lee *et al.* 2011) and a velocity of 4 cm yr^{-1} , which results in 1×10^{10} to $1 \times 10^{12} \text{ N m}^{-1}$. When continental positively buoyant material starts to subduct, the buoyancy force (F_{bo}) becomes important. This force is proportional to the density contrast ($\Delta\rho_c$) between continental lithosphere and the surrounding mantle (Molnar & Gray 1979)

$$F_{\text{bo}} \simeq -\Delta\rho_c g L_c h_c, \quad (15)$$

where L_c is the length of subducted continent, and h_c the thickness of continental crust. Previous studies estimated the buoyancy force at *ca.* 1 – $5 \times 10^{13} \text{ N m}^{-1}$ (Mckenzie 1969; Molnar & Gray 1979) and our models show a buoyancy force of the same order of magnitude in the collision phase. The friction force F_i between the overriding and subducting plates at the subduction channel resists subduction mainly during initiation of subduction, but becomes one order of magnitude smaller than the slab bending force later in model evolution, if the subduction channel has the same viscosity as the mantle (Funicello *et al.* 2003). In our models, the effective viscosity at the plate contact is about 10^{20} Pa s and is on the same order of magnitude as the effective viscosity of the mantle. We therefore ignore this force.

Fig. 15 shows push force (F_p) versus effective slab pull ($F_{\text{sp}} + F_{\text{vr}} + F_{\text{be}} + F_{\text{bo}}$) for four of our numerical models, representative of continental subduction (M2), folding (M7), RT-type dripping (M10) and slab break-off (M27). After about 7 Myr of convergence, enough subduction took place for slab pull to become active in the models. The effective slab pull increases during the oceanic subduction phase. When the subducted oceanic slab reaches the bottom of the model or the whole oceanic slab is subducted and collision starts (at about 14 ± 1 Myr), the effective slab pull decreases. The effective slab pull is initially the main driving force for colder systems [folding model (M7) with $T_{\text{lc}} = 1200 \text{ }^\circ\text{C}$], while the push force is slightly more dominant in warmer systems [RT model (M10) with $T_{\text{lc}} = 1400 \text{ }^\circ\text{C}$]. The push force grows with time for kinematically driven models (M2, M7 and M10), but the growth rate is low in hot and slow systems and high in cold and fast systems. The push force in our dynamic collision model follows the same path as our reference collision model until 10 Myr, and it decreases afterward to a very small value. Fig. 15 shows that stable subduction is the dominant mechanism when the forces are more or less in balance: $F_{\text{sp}} + F_{\text{vr}} + F_{\text{be}} + F_{\text{bo}} \approx F_p$. Folding and thickening become more

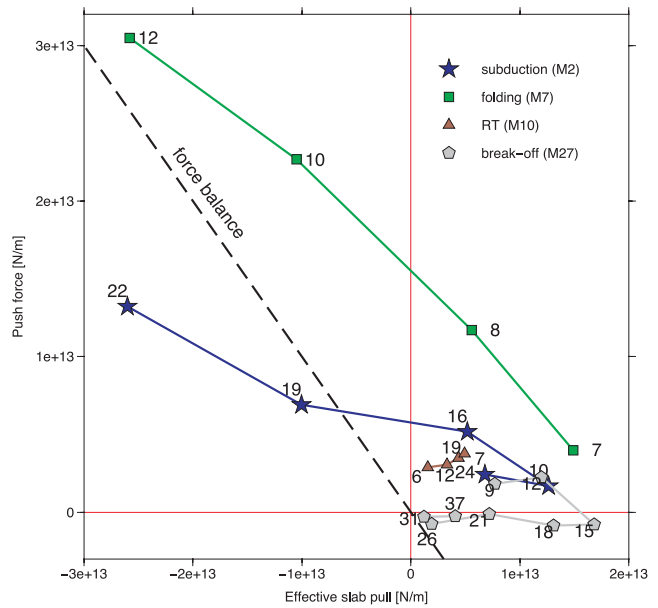


Figure 15. Push force (F_p) versus effective slab pull ($F_{\text{sp}} + F_{\text{vr}} + F_{\text{be}} + F_{\text{bo}}$, Fig. 14) calculated through time for kinematically driven models showing continental stable subduction (M2), folding (M7) and RT-type of dripping (M10) and the dynamic model showing slab break-off (M27). Numbers with symbols are time in Myr, rounded to the nearest whole number. Positive effective slab pull and push force are driving subduction, negative values are resisting.

likely when the continent is pushed more than it is pulled: $F_{\text{sp}} + F_{\text{vr}} + F_{\text{be}} + F_{\text{bo}} < F_p$. If the effective slab pull is stronger than the push force ($F_{\text{sp}} + F_{\text{vr}} + F_{\text{be}} + F_{\text{bo}} > F_p$), slab break-off may occur. Slab break-off exclusively occurred in our dynamic collision model, because the push force in these models is much reduced (to a small contribution by mantle flowing into our artificial mid-ocean ridge at the topright corner of the model).

None of the driving forces (effective slab pull and push force) plays a strong role in hot and slow systems. RT-type of dripping develops in these systems when the growth time of instabilities is on the order of the simulation timescale. The timescale for the formation of lithospheric instabilities (τ_b) can be estimated by (Canright & Morris 1993; Houseman & Molnar 1997)

$$\tau_b = \frac{8\eta_{\text{cl}}}{\Delta\rho_c g h_{\text{cl}}}, \quad (16)$$

where η_{cl} is the effective viscosity of the lower part of the continental lithosphere. The density contrast and thickness do not change much in our models, when the velocity and temperature are varied. The only parameter that effects the timescale is therefore the viscosity. A model with 1 cm yr^{-1} driving velocity and $1400 \text{ }^\circ\text{C}$ mantle temperature (Model M10) has an effective viscosity η_{cl} of approximately 10^{21} Pa s and a RT growth time on the order of 16 Myr, which makes RT-dripping plausible (Fig. 8). However, a model with 4 cm yr^{-1} driving velocity and $1200 \text{ }^\circ\text{C}$ mantle temperature (model M6) with $\eta_{\text{cl}} \sim 10^{22} \text{ Pa s}$ has an RT growth time of ~ 160 Myr, which is outside the timescale of our models.

6 CONCLUSIONS

We have investigated styles of continental collision with 2-D thermomechanical models, which simulate collision after a phase of oceanic subduction. We find that collision style is influenced by

driving velocity, lithospheric temperature, rheological strength of continental crust and lithosphere and the interaction with adjacent plates. We show that:

(1) Stable subduction of continental crust and lithosphere can occur over a wide range of lithosphere temperature (base of lithospheric temperatures of 1250–1350 °C) and driving velocity (1–8 cm yr⁻¹).

(2) Folding is a favoured mechanism for cold and fast systems, whereas RT-type of dripping is more likely to occur in slow and warm systems.

(3) A strong upper crust facilitates subduction of the entire continental crust and part of the overlying sediments to lithospheric depths and promotes folding of the incoming continent, whereas a weak upper crust promotes off-scraping of the upper crust at the trench and formation of an accretionary wedge.

(4) A continent with a weak lower crust can experience accretion of the entire crust at the trench.

(5) Weakening of the lithospheric mantle facilitates RT-type of dripping from the base of the lithosphere.

(6) Variation of the initial density contrast between the oceanic lithosphere and the asthenosphere by 20 kg m⁻³ does not effect collision style.

(7) Slab break-off is facilitated in settings in which the subducting plate does not experience a large push from adjacent plates.

Our study illustrates how a simple force balance can be used to differentiate between stable subduction, continental folding and thickening and slab break-off.

ACKNOWLEDGEMENTS

This study was supported by the Norwegian Research Council through NFR project 180449/V30. We would like to thank Joya Tetreault, Matthieu Quinquis and Zurab Chemia for many stimulating discussions. The constructive reviews of Thibault Duret and Stefan Schmalholz helped our revision. Our models were solved with the numerical code SULEC, which was co-developed between Susanne Buiter and Susan Ellis. Most of our figures were made using GMT (Wessel & Smith 1991).

REFERENCES

Afonso, J.C., Ranalli, G. & Fernández, M., 2007. Density structure and buoyancy of the oceanic lithosphere revisited, *Geophys. Res. Lett.*, **34**, L10302.

Andersen, T.B., Jamtveit, B., Dewey, J.F. & Swenson, E., 1991. Subduction and exhumation of continental crust: major mechanisms during continent-continent collision and orogenic extensional collapse, a model based on the south Norwegian Caledonides, *Terra Nova*, **3**, 303–310.

Andrews, E.R. & Billen, M.I., 2007. Rheologic controls on the dynamics of slab detachment, *Tectonophysics*, **464**, 60–69.

Babeyko, A.Y. & Sobolev, S.V., 2008. High-resolution numerical modeling of stress distribution in visco-elasto-plastic subducting slabs, *Lithos*, **103**, 205–216.

Barazangi, M., Isacks, B.L., Oliver, J., Dubois, J. & Pascal, G., 1973. Descent of lithosphere beneath New Hebrides, Tonga-Fiji and New Zealand: evidence for detached slabs, *Nature*, **242**, 98–101.

Baumann, C., Gerya, T.V. & Connolly, J.A.D., 2010. Numerical modelling of spontaneous slab breakoff dynamics during continental collision, *Geol. Soc. Lond. Spec. Pub.*, **332**, 99–114.

Beaumont, C., Kamp, P.J.J., Hamilton, J. & Fullsack, P., 1996. The continental collision zone, South Island, New Zealand: comparison of geodynamical models and observations, *J. geophys. Res.*, **101**(B2), 3333–3359.

Billen, M.I. & Hirth, G., 2007. Rheologic controls on slab dynamics, *Geochem. Geophys. Geosyst.*, **8**, Q08012.

Blanc, E.J.P., Allen, M.B., Inger, S. & Hassani, H., 2003. Structural styles in the Zagros Simple Folded Zone, Iran, *J. geol. Soc. Lond.*, **160**, 401–412.

Bird, P., 1979. Continental delamination and the Colorado Plateau, *J. geophys. Res.*, **84**, 7561–7571.

Bos, B. & Spiers, C.J., 2002. Fluid-assisted healing processes in gouge-bearing faults: insights from experiments on a rock analogue system, *Pure appl. Geophys.*, **159**, 2537–2566.

Bott, M.H.P., Waghorn, G.D. & Whittaker, A., 1982. Plate boundary forces at subduction zones and trench-arc compression, *Tectonophysics*, **170**, 1–15.

Braeck, S., Podladchikov, Y.Y. & Medvedev, S., 2009. Spontaneous dissipation of elastic energy by self-localizing thermal runaway, *Phys. Rev. E*, **80**, 046105.

Buffett, B.A. & Becker, T.W., 2012. Bending stress and dissipation in subducted lithosphere, *J. geophys. Res.*, **117**, B05413.

Burg, J.P. & Podladchikov, Y., 2000. From buckling to asymmetric folding of the continental lithosphere: numerical modelling and application to the Himalayan syntaxes, *Geol. Soc. Lond. Spec. Pub.*, **170**, 219–236.

Buiter, S. & Ellis, S.M., 2010. The initiation of subduction models, in *AGU Fall Meeting*, D141B-06.

Buiter, S.J.H., 2012. A review of brittle compressional wedge models, *Tectonophysics*, **530–531**, 1–17.

Buiter, S.J.H., Govers, R. & Wortel, M.J.R., 2002. Two-dimensional simulations of surface deformation caused by slab detachment, *Tectonophysics*, **354**, 195–210.

Burov, E. & Yamato, P., 2008. Continental plate collision, P-T-t conditions and unstable vs. stable plate dynamics: insights from thermo-mechanical modelling, *Lithos*, **103**, 178–204.

Canright, D. & Morris, S., 1993. Buoyant instability of a viscous film over a passive fluid, *J. Fluid Mech.*, **255**, 349–372.

Capitanio, F.A., Stegman, D.R., Moresi, L.N. & Sharples, W., 2009. Upper plate controls on deep subduction, trench migrations and deformations at convergent margins, *Tectonophysics*, **483**, 80–92.

Chapman, D.S., 1986. Thermal gradients in the continental crust, *Geol. Soc. Lond. Spec. Pub.*, **24**, 63–70.

Cloetingh, S., Burov, E. & Poliakov, A., 1999. Lithosphere folding: primary response to compression? (from central Asia to Paris Basin), *Tectonophysics*, **18**, 1064–1083.

Crameri, F. & Kaus, B.J.P., 2010. Parameters that control lithospheric-scale thermal localization on terrestrial planets, *Geophys. Res. Lett.*, **37**, L09308.

Culling, W.E.H., 1960. Analytical theory of erosion, *J. Geol.*, **68**, 336–344.

Cuvelier, C., Segal, A. & van Steenhoven, A.A., 1986. *Finite Element Methods and Navier-Stokes Equations*, D. Reidel Publishing Company, Dordrecht, Holland.

Davies, J.H. & Engelder, T., 1985. The role of salt in fold-and-thrust belts, *Tectonophysics*, **119**, 67–88.

Davies, J.H. & von Blanckenburg, F., 1995. Slab breakoff: a model of lithosphere detachment and its test in the magmatism and deformation of collisional orogens, *Earth planet. Sci. Lett.*, **129**, 85–102.

De Franco, R., Govers, R. & Wortel, R., 2008. Dynamics of continental collision: influence of the plate contact, *Geophys. J. Int.*, **174**, 1101–1120.

Dewey, J.F. & Burke, K.C.A., 1973. Tibetan, Variscan, and Precambrian basement reactivation: products of continental collision, *J. Geol.*, **81**, 683–692.

Ding, L., Kapp, P., Zhong, D. & Deng, W., 2003. Cenozoic volcanism in Tibet: evidence for a transition from oceanic to continental subduction, *J. Petrol.*, **44**, 1833–1865.

Duret, T., Gerya, T.V. & May, D.A., 2011. Numerical modelling of spontaneous slab break-off and subsequent topographic response, *Tectonophysics*, **502**, 244–256.

Duret, T., Schmalholz, S.M. & Gerya, T.V., 2012. Dynamics of slab detachment, *Geochem. Geophys. Geosyst.*, **13**, Q03020.

Faccenda, M., Minelli, G. & Gerya, T.V., 2008. Coupled and decoupled regimes of continental collision: numerical modeling, *Earth planet. Sci. Lett.*, **278**, 337–349.

- Fuchs, K. *et al.*, 1979. The Romanian earthquake of March 4, 1977. II. Aftershocks and migration of seismic activity, *Tectonophysics*, **53**, 225–247.
- Fullsack, P., 1995. An arbitrary Lagrangian-Eulerian formulation for creeping flows and its applications in tectonic models, *Geophys. J. Int.*, **120**, 1–23.
- Funiciello, F., Faccenna, C., Giardini, D. & Regenauer-Lib, K., 2003. Dynamics of retreating slabs: 2. Insights from three-dimensional laboratory experiments, *J. geophys. Res.*, **108**(B4), 2207.
- Gerya, T.V., Yuen, D.A. & Maresch, W.V., 2004. Thermo-mechanical modelling of slab detachment, *Earth planet. Sci. Lett.*, **226**, 101–116.
- Gleason, G.C. & Tullis, J., 1995. A flow law for dislocation creep of quartz aggregates determined with the molten salt cell, *Tectonophysics*, **247**, 1–23.
- Guillaume, B., Martinod, J. & Espurt, N., 2009. Variations of slab dip and overriding plate tectonics during subduction: insights from analogue modeling, *Tectonophysics*, **463**, 167–174.
- Hacker, B.R., 2006. Pressure and temperature of ultrahigh-pressure metamorphism: implications for UHP tectonics and H₂O in subducting slabs, *Int. geol. Rev.*, **48**, 1053–1066.
- Hacker, B.R., Andersen, T.B., Johnston, S., Kylander-Clark, A.R.C., Peterman, E.M., Walsh, E.O. & Young, D., 2010. High-temperature deformation during continental-margin subduction & exhumation: the ultrahigh-pressure Western Gneiss Region of Norway, *Tectonophysics*, **480**, 149–171.
- Hafkenscheid, E., Wortel, M.J.R. & Spakman, W., 2006. Subduction history of the Tethyan region derived from seismic tomography and tectonic reconstructions, *J. geophys. Res.*, **111**, B08401.
- Hirth, G. & Kohlstedt, D., 2003. Rheology of the upper mantle and mantle wedge: a view from the experimentalists, in *Inside the Subduction Factory*, Geophysical Monograph Series, Vol. 138, pp. 83–105. ed. Eiler, J., American Geophysical Union.
- Huiqi, L., McClay, K.R. & Powell, D., 1992. Physical models of thrust wedges, in *Thrust Tectonics*, pp. 71–81, ed. McClay, K.R., Chapman and Hall, New York.
- Houseman, G.A. & Molnar, P., 1997. Gravitational (Rayleigh-Taylor) instability of a layer with nonlinear viscosity and convergence thinning of continental lithosphere, *Geophys. J. Int.*, **128**, 125–150.
- Jamtveit, B., Carswell, D.A. & Mearns, E.W., 1991. Chronology of Norwegian garnet peridotites/pyroxenites, *J. Metamorph. Geol.*, **9**, 125–139.
- Kaus, B.J.P. & Podladchikov, Y.Y., 2006. Initiation of localized shear zones in viscoelastoplastic rocks, *J. geophys. Res.*, **111**, B04412.
- Kaus, B.J.P., Mühlhaus, H. & May, D.A., 2010. A stabilization algorithm for geodynamic numerical simulations with a free surface, *Phys. Earth planet. Inter.*, **181**, 12–20.
- Lee, C.-K., Han, S.-C. & Steinberger, B., 2011. Influence of variable uncertainties in seismic tomography models on constraining mantle viscosity from geoid observations, *Phys. Earth planet. Inter.*, **184**, 51–62.
- Leech, M.L., Singh, S., Jain, A.K., Klempner, S.L. & Manickavasagam, R.M., 2005. The onset of India-Asia continental collision: early, steep subduction required by the timing of UHP metamorphism in the western Himalaya, *Earth planet. Sci. Lett.*, **234**, 83–97.
- Li, L. & Liao, X., 2002. Slab break-off depth: a slowdown subduction model, *Geophys. Res. Lett.*, **29**, 1041–1044.
- Li, Z.H., Gerya, T.V. & Burg, J.P., 2010. Influence of tectonic overpressure on P-T paths of HP-UHP rocks in continental collision zones: thermomechanical modelling, *J. Metamorph. Geol.*, **28**, 227–247.
- Li, Z.H., Xu, Z.Q. & Gerya, T.V., 2011. Flat versus steep subduction: contrasting modes for the formation and exhumation of high- to ultrahigh-pressure rocks in continental collision zones, *Earth planet. Sci. Lett.*, **301**, 65–77.
- Luth, S., Willingshofer, E., Sokoutis, D. & Cloetingh, S., 2010. Analogue modelling of continental collision: influence of plate coupling on mantle lithosphere subduction, crustal deformation and surface topography, *Tectonophysics*, **484**, 87–102.
- Mandl, G., 1988. *Mechanics of Tectonic Faulting, Developments in Structural Geology*, ed. Zwart, H.J., Elsevier, Amsterdam, 407pp.
- Mancktelow, N.S., 2008. Tectonic pressure: theoretical concepts and modelled examples, *Lithos*, **103**, 149–177.
- Mckenzie, D.P., 1969. Speculations on the consequences and causes of plate motions, *Geophys. J. R. astr. Soc.*, **18**, 1–32.
- Molnar, P. & Gray, D., 1979. Subduction of continental lithosphere: some constraints and uncertainties, *Geology*, **7**, 58–62.
- Molnar, P. & Tapponnier, P., 1975. Cenozoic tectonics of Asia: effects of a continental collision, *Science*, **189**, 419–426.
- Parsons, B. & Richter, M., 1980. A relation between the driving force and geoid anomaly associated with mid-ocean ridges, *Earth planet. Sci. Lett.*, **51**, 445–450.
- Pascal, G., Bubols, J., Barazangi, M., Isacks, B.L. & Oliver, J., 1973. Seismic velocity anomalies beneath the New Hebrides Island Arc: evidence for a detached slab in the upper mantle, *J. geophys. Res.*, **78**, 6998–7004.
- Pelletier, D., Fortin, A. & Camarero, R., 1989. Are FEM solutions of incompressible flows really incompressible? (or how simple flows can cause headaches!), *Int. J. Num. Methods Fluid*, **9**, 99–112.
- Pfiffner, O.A., Frei, W., Valasek, P., Stäubli, M., Levato, L., DuBois, L., Schmid, S.M. & Smithson, S.B., 1990. Crustal shortening in the Alpine Orogen: results from deep seismic reflection profiling in the eastern Swiss Alps, *Tectonophysics*, **9**, 1327–1355.
- Pysklywec, R.N., 2006. Surface erosion control on the evolution of the deep lithosphere, *Bull. geol. Soc. Am.*, **34**, 225–228.
- Pysklywec, R.N. & Beaumont, C., 2004. Intraplate tectonics: feedback between radioactive thermal weakening and crustal deformation driven by mantle lithosphere instabilities, *Earth planet. Sci. Lett.*, **221**, 275–292.
- Pysklywec, R.N. & Cruden, A.R., 2004. Coupled crust-mantle dynamics and intraplate tectonics: two-dimensional numerical and three-dimensional analogue modeling, *Geochem. Geophys. Geosystems.*, **5**, Q10003.
- Pysklywec, R.N., Beaumont, C. & Fullsack, P., 2000. Modeling the behavior of the continental mantle lithosphere during plate convergence, *Geology*, **28**, 655–658.
- Quinquis, M.E.T., Buiter, S.J.H. & Ellis, S., 2011. The role of boundary conditions in numerical models of subduction zone dynamics, *Tectonophysics*, **497**, 57–70.
- Ranalli, G., 1995. *Rheology of the Earth*, 2nd edn, Chapman & Hall, London, 413pp.
- Ranalli, G., Pellegrini, R. & D’Offizi, S., 2000. Time dependence of negative buoyancy and the subduction of continental lithosphere, *J. Geodyn.*, **30**, 539–555.
- Regenauer-Lieb, K. & Yuen, D., 2003. Modeling shear zones in geological and planetary science: solid- and fluid-thermal-mechanical approaches, *Earth Sci. Rev.*, **63**, 295–349.
- Rice, J., 1992. Fault stress states, pore pressure distributions and the weakening of the San Andreas fault, in *Fault Mechanics and the Transport Properties of Rocks: A Festschrift in Honor of W. F. Brace*, pp. 475–504, eds Evans, B. & Wong, T.-F., Academic Press, New York.
- Roecker, S.W., Yeh, Y.H. & Tsai, Y.B., 1987. Three-dimensional P and S wave velocity structures beneath Taiwan: deep structure beneath an arc-continent collision, *J. geophys. Res.*, **92**, 547–570.
- Rybacki, E., Gottschalk, M., Wirth, R. & Dresen, G., 2006. Influence of water fugacity and activation volume on the flow properties of fine-grained anorthite aggregates, *J. geophys. Res.*, **111**, B03203.
- Schellart, W.P., 2005. Influence of the subducting plate velocity on the geometry of the slab and migration of the subduction hinge, *Geochem. Geophys. Geosyst.*, **231**, 197–219.
- Schellart, W.P., 2008. Kinematics and flow patterns in deep mantle and upper mantle subduction models: influence of the mantle depth and slab to mantle viscosity ratio, *Earth planet. Sci. Lett.*, **9**, Q03014.
- Schenk, O. & Gärtner, K., 2004. Solving unsymmetric sparse systems of linear equations with PARDISO, *Future Gener. Comput. Syst.*, **20**, 475–487.
- Schmalholz, S.M., Podladchikov, Y.Y. & Burg, J.P., 2002. Control of folding by gravity and matrix thickness: implications for large-scale folding, *J. geophys. Res.*, **107**(B1).

- Selzer, C., Buitert, S.J.H. & Pfiffner, O.A., 2008. Numerical modeling of frontal and basal accretion at collisional margins, *Tectonophysics*, **27**, TC3001.
- Steinberger, B. & Calderwood, A.R., 2006. Models of large-scale viscous flow in the Earth's mantle with constraints from mineral physics and surface observations, *Geophys. J. Int.*, **167**, 1461–1481.
- Stockmal, G.S., Beaumont, C., Nguyen, M. & Lee, B., 2007. Mechanics of thin-skinned fold-and-thrust belts: insights from numerical models, *Bull. geol. Soc. Am.*, **433**, 63–98.
- Tapponnier, P., Peltzer, G. & Armijo, R., 1986. On the mechanics of the collision between India and Asia, *Geol. Soc. Lond. Spec. Pub.*, **19**, 113–157.
- Toth, J. & Gurnis, M., 1998. Dynamics of subduction initiation at preexisting fault zones, *J. geophys. Res.*, **103**, 18 053–18 067.
- Toussaint, G., Burov, E. & Jolivet, L., 2004a. Continental plate collision: unstable vs. stable slab dynamics, *Geology*, **32**, 33–36.
- Toussaint, G., Burov, E. & Avouac, J.P., 2004b. Tectonic evolution of a continental collision zone: a thermomechanical numerical model, *Tectonophysics*, **23**, TC6003.
- Turcotte, D.L. & Schubert, G., 2002. *Geodynamics*, 2nd edn, Cambridge University Press, New York, 848pp.
- van den Berg, A.P., van Keken, P.E. & Yuen, D.A., 1993. The effects of a composite non-Newtonian and Newtonian rheology on mantle convection, *Geophys. J. Int.*, **115**, 62–78.
- van Hunen, J. & Allen, M.B., 2011. Continental collision and slab break-off: a comparison of 3-D numerical models with observations, *Earth planet. Sci. Lett.*, **302**, 27–37.
- Vrijmoed, J.C., Podladchikov, Y.Y., Andersen, T.B. & Hartz, H., 2009. An alternative model for ultra-high pressure in the Svartberget Fe-Ti garnet-peridotite, Western Gneiss Region, Norway, *Eur. J. Mineral.*, **21**, 1119–1133.
- von Blanckenburg, F. & Davies, J., 1995. Slab breakoff: a model for syn-collisional magmatism and tectonics in the Alps, *Tectonophysics*, **14**, 120–131.
- Warren, C.J., 2013. Exhumation of (ultra-)high pressure terranes: concepts and mechanisms, *Solid Earth*, **4**, 75–92.
- Warren, C.J., Beaumont, C. & Jamieson, R.A., 2008. Modelling tectonic styles and ultra-high pressure (UHP) rock exhumation during the transition from oceanic subduction to continental collision, *Earth planet. Sci. Lett.*, **267**, 129–145.
- Wessel, P. & Smith, W.H.F., 1991. Free software help map and display data, *EOS, Trans. Am. geophys. Un.*, **72**, 445–446.
- Wilks, K.R. & Carter, N.L., 1990. Rheology of some continental lower crustal rocks, *Tectonophysics*, **182**, 57–77.
- Wortel, M.J.R. & Spakman, W., 2000. Subduction and slab detachment in the Mediterranean-Carpathian Region, *Science*, **290**(5498), 1910–1917.
- Ye, K., Cong, B. & Ye, D., 2000. The possible subduction of continental material to depths greater than 200 km, *Nature*, **407**, 734–736.
- Zienkiewicz, O.C. & Taylor, R.L., 2000. *The Finite Element Method*, Volume 3: Fluid Dynamics, 5th edn, Butterworth-Heinemann, 435pp.

APPENDIX A: THE INFLUENCE OF MANTLE TEMPERATURE

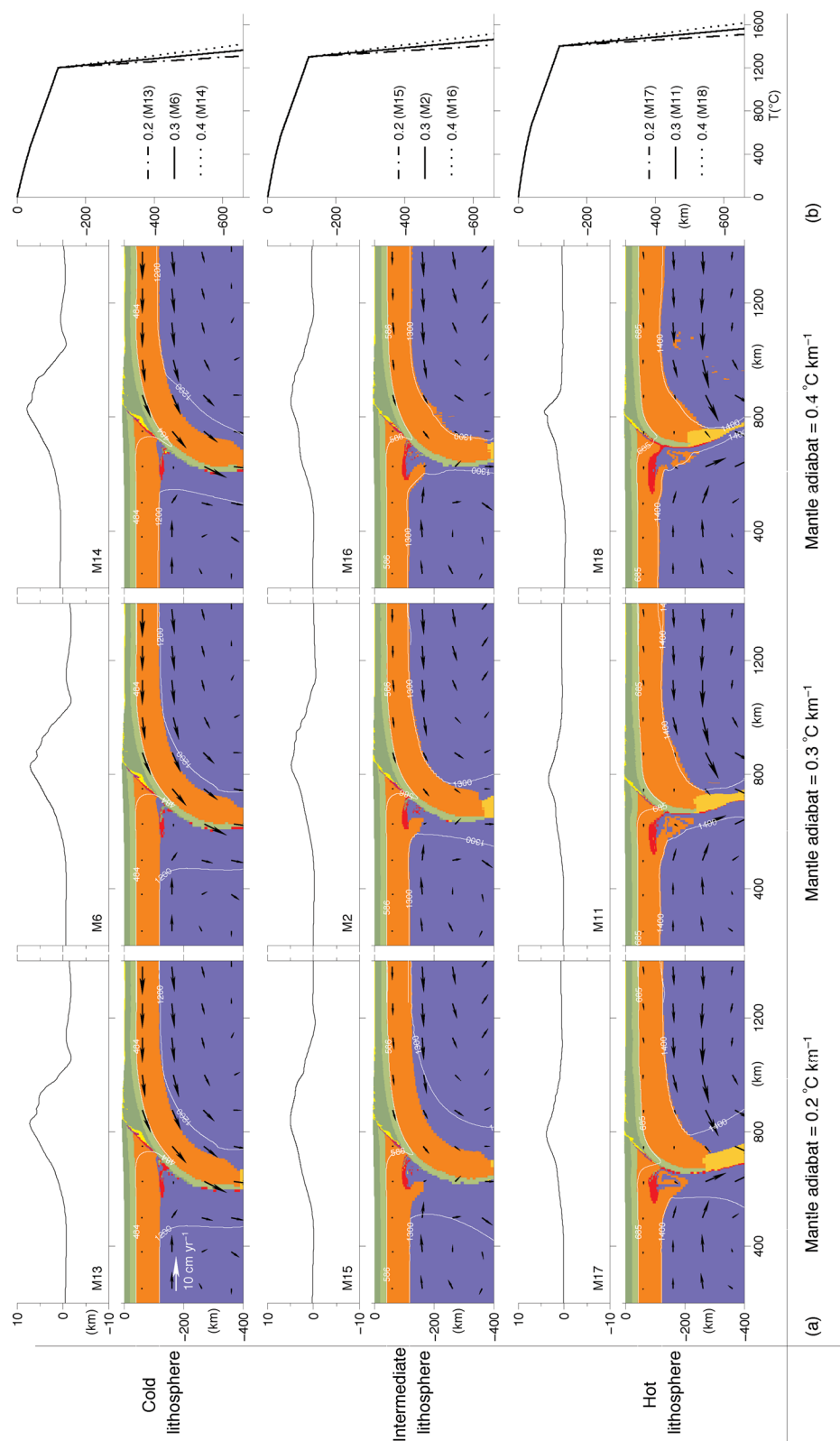


Figure A1. (a) Kinematically driven collision models showing the effects of variations in mantle adiabat for a cold ($T_{lc} = 1200\text{ }^\circ\text{C}$), intermediate ($T_{lc} = 1300\text{ }^\circ\text{C}$) and hot lithosphere ($T_{lc} = 1400\text{ }^\circ\text{C}$). The mantle adiabat is varied between 0.2, 0.3 and $0.4\text{ }^\circ\text{C km}^{-1}$. The panels show material and velocity fields after 24 Myr of convergence, with surface topography at the top. (b) Initial continental geotherms.